iScience

CellPress
OPEN ACCESS

Article

Cytochrome *c* prompts the recruitment of its nuclear partners SET/TAF-Iβ and NPM1 into biomolecular condensates

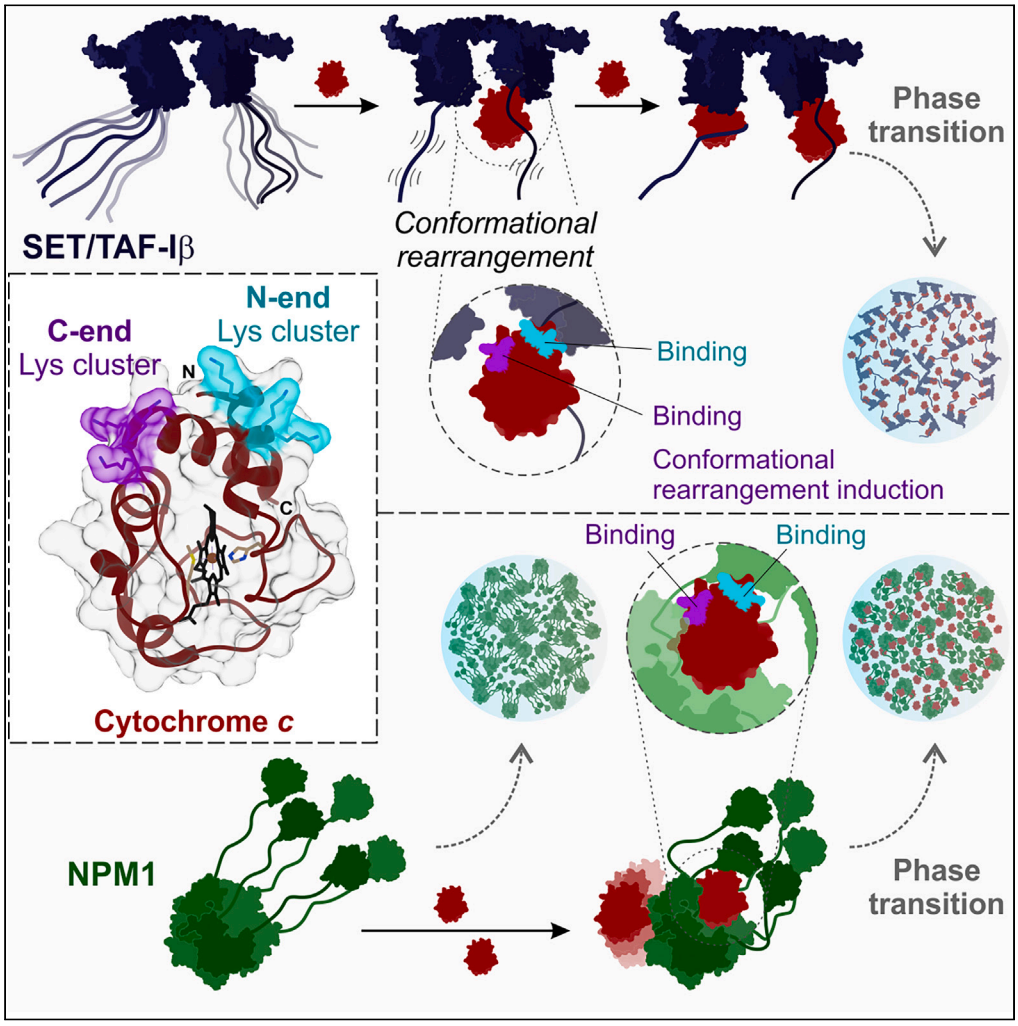

Miguel Á. Casado-Combreras, Adrián Velázquez-Campoy, Marlène Martinho, Valérie Belle, Miguel A. De la Rosa, Irene Díaz-Moreno

idiazmoreno@us.es

Highlights

Cytochrome *c* and SET/TAF-Iβ phase separate together

Cytochrome *c* is a protein with sequence-encoded phase-separation properties

Cytochrome *c*-driven dynamical rearrangement of SET/TAF-Iβ drives phase transition

Selective cytochrome *c* mobility inside condensates harboring SET/TAF-Iβ or NPM1

Casado-Combreras et al., iScience *27*, 110435
August 16, 2024
https://doi.org/10.1016/j.isci.2024.110435

iScience

CellPress
OPEN ACCESS

Article

Cytochrome *c* prompts the recruitment of its nuclear partners SET/TAF-Iβ and NPM1 into biomolecular condensates

Miguel Á. Casado-Combreras,[1] Adrián Velázquez-Campoy,[2,3,4,5] Marlène Martinho,[6] Valérie Belle,[6] Miguel A. De la Rosa,[1] and Irene Díaz-Moreno[1,7,*]

SUMMARY

Compartmentalization of proteins by liquid-liquid phase separation (LLPS) is used by cells to control biochemical reactions spatially and temporally. Among them, the recruitment of proteins to DNA foci and nucleolar trafficking occur by biomolecular condensation. Within this frame, the oncoprotein SET/TAF-Iβ plays a key role in both chromatin remodeling and DNA damage response, as does nucleophosmin (NPM1) which indeed participates in nucleolar ribosome synthesis. Whereas phase separation by NPM1 is widely characterized, little is known about that undergone by SET/TAF-Iβ. Here, we show that SET/TAF-Iβ experiences phase separation together with respiratory cytochrome *c* (Cc), which translocates to the nucleus upon DNA damage. Here we report the molecular mechanisms governing Cc-induced phase separation of SET/TAF-Iβ and NPM1, where two lysine-rich clusters of Cc are essential to recognize molecular surfaces on both partners in a specific and coordinated manner. Cc thus emerges as a small, globular protein with sequence-encoded heterotypic phase-separation properties.

INTRODUCTION

Biomolecular condensates have attracted a wealth of research interest in recent years as an important physiological phenomenon for the spatial-temporal regulation of many biochemical processes.[1] Such biomolecular condensates are supramolecular, micron-sized structures formed by proteins and often nucleic acids that reorganize from a diluted into a—usually liquid-like—dense phase, through a process known as liquid-liquid phase separation (LLPS).[1,2] Condensates lead the enrichment or exclusion of certain macromolecules, favoring or restricting different biochemical events.[3–5] Indeed, LLPS is the primary basis for the formation of membraneless organelles (MLOs)—such as nucleoli, P-granules or nuclear speckles and paraspeckles[6–8]—as well as other transient compartments—including DNA damage foci or stress granules.[3,9–11]

The formation of biomolecular condensates requires the onset of multivalent interactions, established by proteins that usually are multidomain or contain intrinsically disordered regions (IDRs).[3,12] Such interactions encompass weak physical crosslinks, including electrostatic forces, π-π stacking, cation-π, hydrophobic interactions, or hydrogen bonds (H-bonds) formation.[13–17] In particular, when the attraction between two macromolecules is based on electrostatic complementarity, they can undergo spontaneous phase transitions that are known as electrostatic complex coacervation.[18,19] The driving forces for such kind of phase transitions actually consist of long-range electrostatic interactions driving the association between oppositely charged macromolecules, along with counterion release.[20] Therefore, electrostatic coacervates are dissolved at high ionic strength.[21] Usually, complex coacervation gives rise to short-range interactions that stabilize LLPS or trigger other processes such as percolation or gelation.[19,20] Currently, the distinction between LLPS and other percolation processes that can be coupled to it, such as gelation or solid-transitions, is well established based on the viscoelastic and dynamic properties of condensates. The term phase separation (PS) will then more accurately refer to condensation processes in a general manner.[22]

In proteins, residues capable of forming such associations are often distributed within patches or sequence repeats that confer site-specific associativity to the protein.[23] Such interacting motifs—or even particular residues—are known as "stickers" and they are interspersed with non-interacting residues or "spacers".[20,24] While stickers essentially determine the type and strength of interactions that can be established,[20,25] spacers are critical in determining the conformational landscape, orientation and availability of stickers in the case of both IDRs

[1]Institute for Chemical Research (IIQ), Scientific Research Center "Isla de la Cartuja" (cicCartuja), University of Seville - CSIC, Seville, Spain
[2]Institute for Biocomputation and Physic of Complex Systems (BIFI), Joint Unit GBsC-CSIC-BIFI, University of Zaragoza, Zaragoza, Spain
[3]Departament of Biochemistry and Molecular and Cellular Biology, University of Zaragoza, Zaragoza, Spain
[4]Institute for Health Research Aragón (IIS Aragon), Zaragoza, Spain
[5]Centre for Biomedical Research Network of Hepatic and Digestive Diseases (CIBERehd), Madrid, Spain
[6]Aix Marseille University, CNRS, BIP, Bioénergétique et Ingénierie des Protéines, IMM, IM2B, Marseille, France
[7]Lead contact
*Correspondence: idiazmoreno@us.es
https://doi.org/10.1016/j.isci.2024.110435

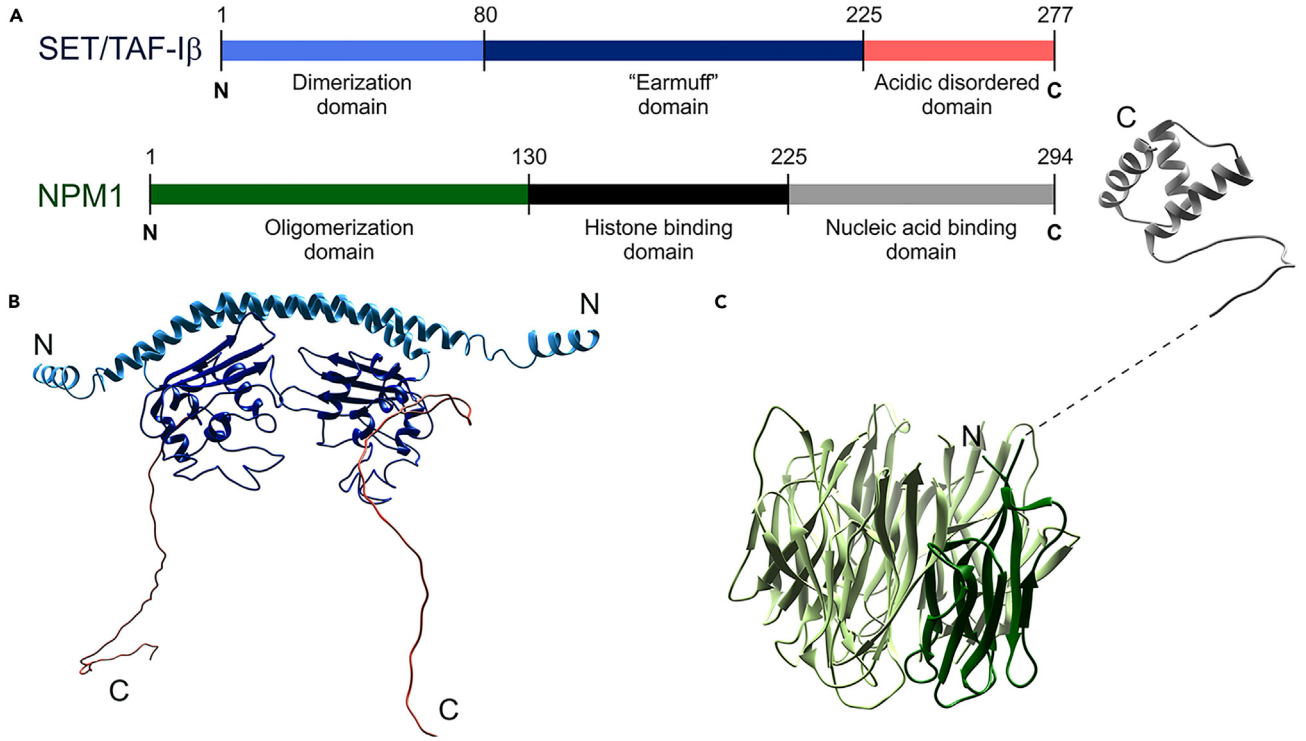

Figure 1. Structural architecture of SET/TAF-Iβ and NPM1

(A) Domain organizations and (B and C) ribbon representation of structural models for (B) SET/TAF-Iβ and (C) NPM1. For the SET/TAF-Iβ model, dimerization domain (residues 1–80) is represented in light blue, the "earmuff" domain (81–225) in dark blue, and the acidic disordered domain (226–277) in coral. The structural model was built using MODELLER[58] to trace the earmuff loops and C-terminal unstructured stretches, which were absent in the crystallographic structure (PDB entry 2E50[39]). For the NPM1 model, oligomerization domains forming a pentamer unit are represented in green (residues 1–130, PDB entry 4N8M[55]), highlighting one monomer in dark green. The disordered histone-binding domain (residues 131–225) has not been modeled. The C-terminal nucleic-acid binding domain (residues 226–294, PDB entry 2LLH[59]) is in gray.

or intrinsically folded domains and globular proteins.[26] Specific sticker distributions and sequence features—usually referred to as "molecular grammars"—have been profoundly investigated to establish the molecular tenets of PS, especially for IDRs.[14,19,20,27–29] Although proteins with a defined folding are rarely involved in LLPS processes,[30] featuring sticker patches with specific orientations provides them multivalency and then, the ability to undergo PS.[26,31] This is the case of cytochrome *c* (Cc), a small and globular lysine-rich polypeptide that exemplifies the kind of particles described above.

Cc is a small globular hemeprotein that is translocated from the mitochondria to the nucleus under conditions of DNA damage and participates in the stress response through a network of interactions.[32,33] Soon after DNA injury, Cc is capable to be integrated into the nucleolus and interact with nucleophosmin (NPM1), which is an abundant nucleolar protein involved in ribosome biogenesis. Then, Cc displaces the alternative reading frame (ARF) tumor suppressor out of the nucleolus, which in turn prevents proteasomal degradation of p53 by sequestering human double-minute 2 protein (HDM2).[34,35] Nuclear Cc has also been reported to target SET/TAF-Iβ,[32] an oncoprotein with histone chaperone activity involved in several biological processes,[36–38] including chromatin remodeling[39,40] and DNA damage response (DDR).[41,42] In particular, the ability of Cc to hinder SET/TAF-Iβ nucleosome assembly activity[43] and also its role as protein phosphatase 2A (PP2A) inhibitor[44,45] have been characterized. Although SET/TAF-Iβ has not been reported to be involved in LLPS processes to date, it is a well-known player in DNA damage foci—as the well-known phase-separating factors fused-in-sarcoma (FUS) or p53-binding protein 1 (53BP1)[3,17,46,47]—where SET/TAF-Iβ retains DNA repair regulatory factors, such as heterochromatin protein 1 (HP1) family. HP1, which regulates DNA repair[41] and heterochromatin organization, exerts its function within LLPS compartments.[48,49] Within this frame, questions arise whether SET/TAF-Iβ undergoes PS in DNA foci.

SET/TAF-Iβ is a homo-dimer formed by coiled-coil interactions between the N-terminal α-helical domains present in each monomer (Figures 1A and 1B). Each domain is followed by a globular region, usually called the "earmuff" motif, and a C-end IDR consisting of repeats of Asp and Glu.[39] Both "earmuff" motifs and IDRs have been identified as the carriers of histone chaperone activity[39,50] and Cc-binding ability.[43,44] NPM1 is a homo-pentamer assembled by the N-terminal domains, which present a β-barrel architecture (Figures 1A and 1C). This is followed by a histone-binding domain, which is an IDR composed of alternating acidic and basic stretches, connected to a small globular C-end DNA binding domain.[51] NPM1 has been described as a "scaffold" molecule[52] of the nucleolus, being essential for its structural

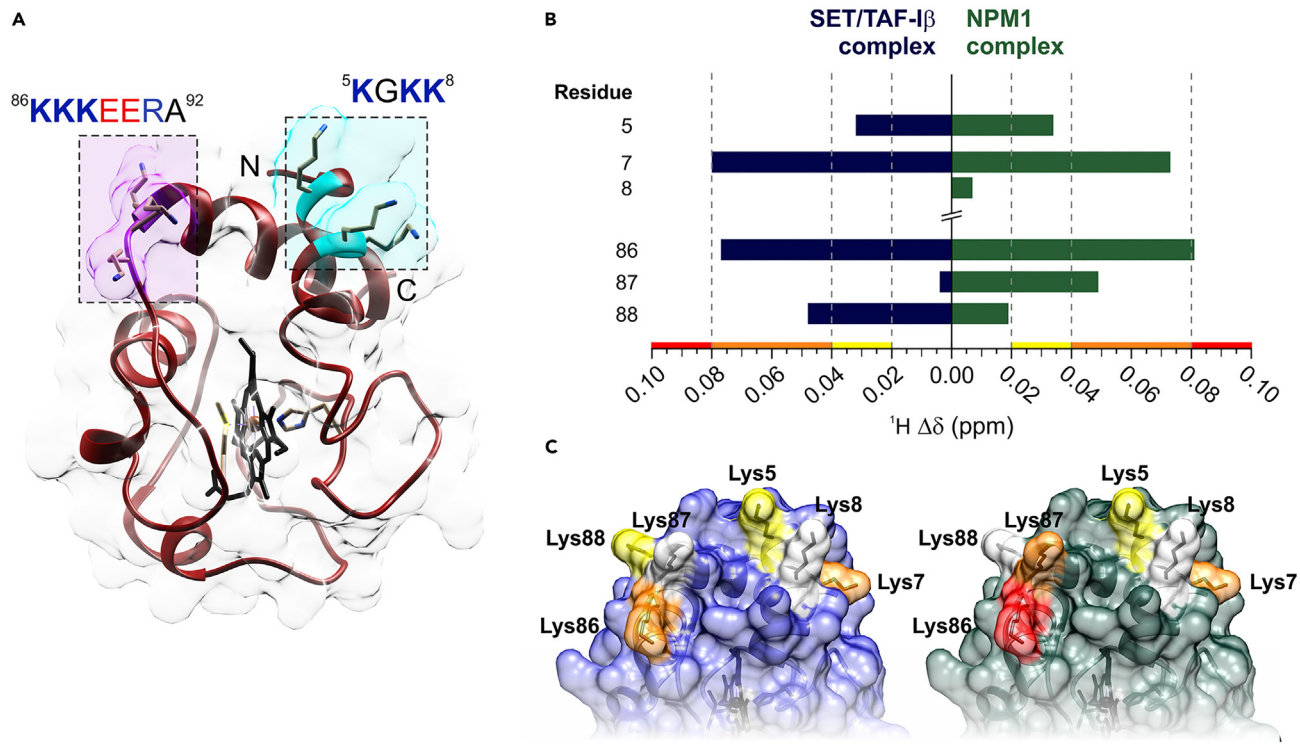

Figure 2. Cytochrome *c* lysine clusters involved in the interaction with SET/TAF-Iβ and NPM1

(A) Ribbon representation of C*c* (PDB entry 2N9I[64]). C*c* Lys clusters mutated in this study are shown. The N-terminal cluster containing Lys5, Lys7, and Lys8 is shown in cyan. The C-terminal cluster with Lys86, Lys87, and Lys88 is highlighted in purple. The last Lys-stretch is part of the minimal unit of C*c* defined as a cell-penetrating peptide (residues 86–92[63]).

(B) ^{1}H chemical-shift perturbations (^{1}H Δδ) of amide resonances of Lys residues of ^{15}N-labelled C*c* upon titrating with SET/TAF-Iβ (*left*) or NPM1 (*right*), inferred from ^{1}H-^{15}N HSQC NMR spectra.[34,43] Bars are colored according to ^{1}H Δδ (ppm) values: white for <0.020, yellow for ≤0.040, orange for ≤0.080, and red for ≤0.100.

(C) Surface mapping of ^{1}H Δδ underwent by Lys amide residues located at the N-end and C-end clusters of C*c* (PDB entry 2N9I[64]) upon complex formation with SET/TAF-Iβ (*left*) or NPM1 (*right*). Lys are colored following the same code as in panel B.

integrity and one of the main responsible for its assembly and function.[53,54] In fact, the NPM1 pentameric state is important for its nucleolar localization.[55] Pentamerization, along with DNA binding domains, powers NPM1 multivalency and allows it to undergo LLPS, mainly through its IDR enriched not only in "D/E-tracts," but also in "K-blocks".[14,54,55] NPM1 "D/E-tracts" and "K-blocks", together with adjacent Arg residues (Figure S1), allow the assembly of NPM1 coacervates by establishing homo-[56] and heterotypic interactions, either with other NPM1 molecules or with other partners, such as ARF[57] or C*c*.[34]

Our former research work showed that C*c* binds both SET/TAF-Iβ and NPM1 proteins mainly through the surface amino acids surrounding the heme group.[34,43,44] This surface is characterized by a prominent positive electrostatic potential, as it hosts 18 lysine amino acids out of the total 104 C*c* residues. Such lysine residues play a pivotal role in the interactions involving C*c*, most of which are based on electrostatics.[32,60,61] Most of these lysines are exposed to the solvent and grouped into clusters. Two of these K-blocks deserve a special focus: (I) the cluster composed of Lys5, Lys7 and Lys8 at the N-end of α_1-helix; and (II) the cluster comprising Lys86, Lys87 and Lys88 at the C-terminal α_4-helix (Figure 2A). For simplicity, we will refer to them as the N-terminal and C-terminal K-blocks, respectively. Both K-blocks have been shown to participate in the binding interface with both SET/TAF-Iβ and NPM1,[34,43] even though they show different chemical-shift perturbations (CSPs) in each complex (Figures 2B and 2C). It is noteworthy that the N-terminal K-block of C*c* exhibits a similar topology and sidechain orientation as the C-terminal domain of HDM2 (Figure S2) that, upon being recognized by NPM1, prevents the binding of HDM2 to p53, thus stabilizing the tumor suppressor protein.[62] Furthermore, the segment comprising residues 86 to 101—which contains the aforementioned C-terminal K-block—has been reported to be the minimal C*c* unit capable of inducing caspase activation[63] and sufficient to define bioactive cell penetrating peptides with which the hemeprotein could be directed toward the nucleus.[63]

In this work, we first report the ability of the oncoprotein SET/TAF-Iβ to phase separate together with C*c*. We use this model system, along with the previously reported NPM1:C*c* condensates, to delve deep into the molecular mechanisms by which the aforementioned K-blocks in C*c* mediate heterotypic PS transitions by modulating (I) intrinsic hemeprotein structural and dynamic properties, and (II) recognition modes toward nuclear partners.

RESULTS

SET/TAF-Iβ forms electrostatic condensates with cytochrome *c* by liquid-liquid phase co-separation

The recruitment of DDR factors, such as SET/TAF-Iβ,[41] to DNA foci occurs through LLPS mechanisms.[65] Given the ability of mitochondrial, respiratory Cc to reach the cell nucleus in response to DNA lesions and to interfere with the SET/TAF-Iβ functioning,[43] we hypothesize that both Cc and SET/TAF-Iβ proteins are capable of assembling liquid-like condensates.

A titration of SET/TAF-Iβ with Cc resulted in the formation of phase-separated liquid droplets that hosted both proteins (Figure 3A). This process was clearly observed when the molar SET/TAF-Iβ:Cc ratio was 1:8. Previously, we reported that Cc recognizes two binding sites in

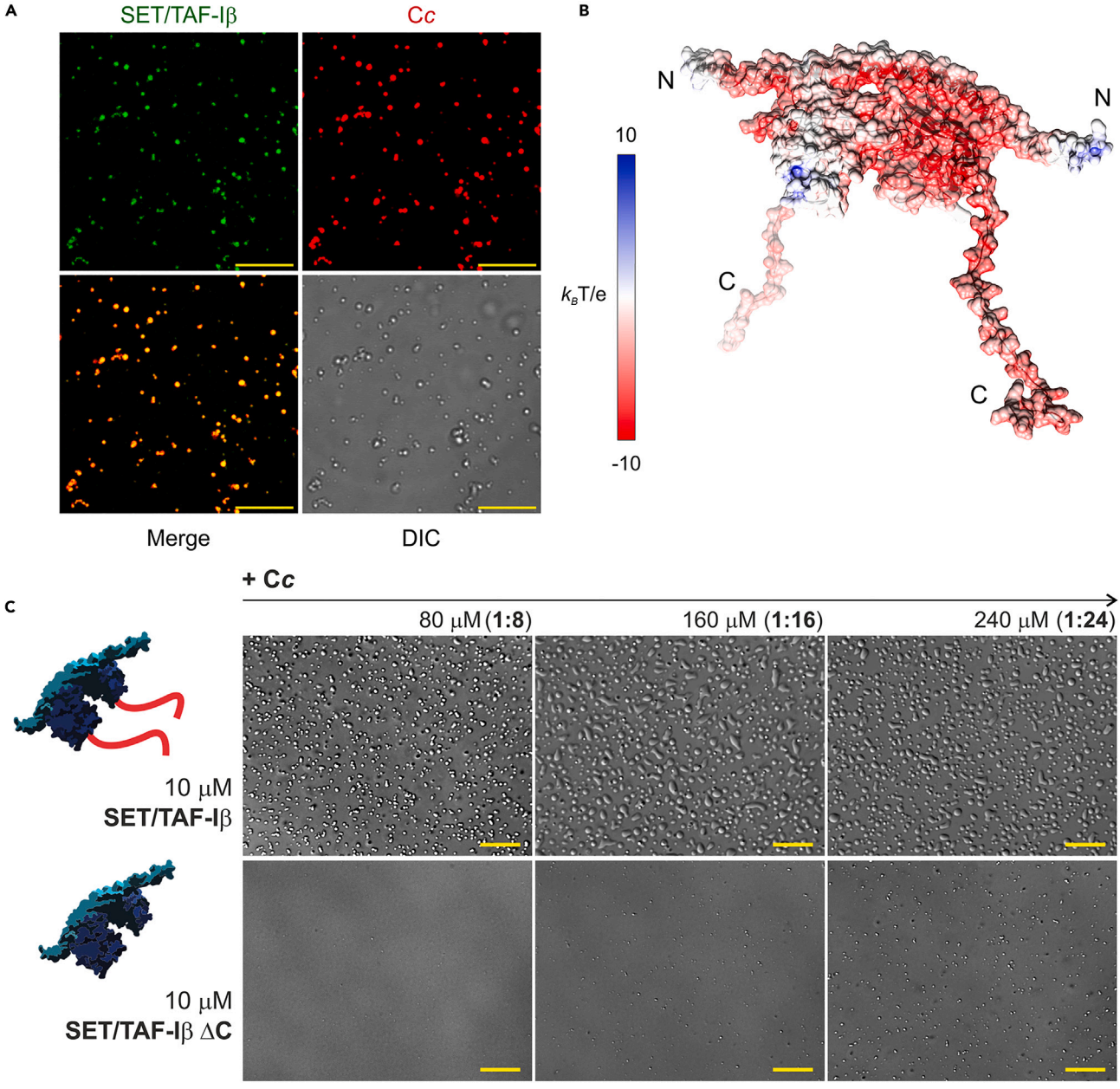

Figure 3. SET/TAF-Iβ phase separates upon binding to cytochrome *c*

(A) Fluorescence confocal microscopy images of phase separation by 10 μM SET/TAF-Iβ with 80 μM Cc. SET/TAF-Iβ was labeled with Oregon Green 488 (green) and Cc, with Texas Red-succinimidyl ester (red). Scale bars: 10 μm.

(B) Electrostatic surface potential map of SET/TAF-Iβ, calculated at 15 mM ionic strength.

(C) DIC microscopy images of droplets formed by 10 μM either SET/TAF-Iβ or SET/TAF-Iβ ΔC with 80, 160, or 240 μM Cc (chaperone:Cc molar ratios of 1:8, 1:16 and 1:24). Scale bars: 30 μm.

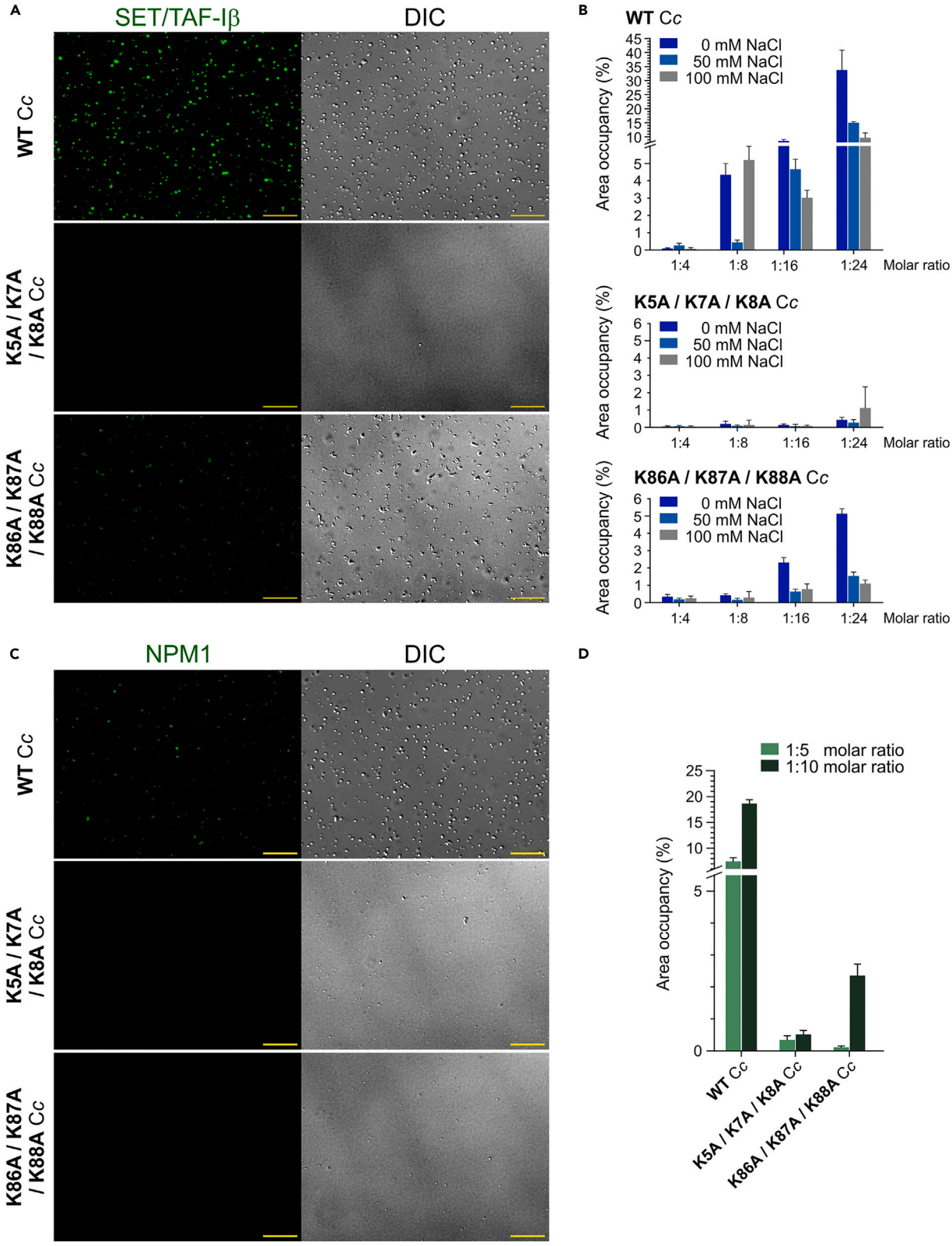
A
SET/TAF-Iβ
DIC
WT Cc
K5A / K7A / K8A Cc
K86A / K87A / K88A Cc
B
WT Cc
0 mM NaCl
50 mM NaCl
100 mM NaCl
Area occupancy (%)
1:4
1:8
1:16
1:24
Molar ratio
K5A / K7A / K8A Cc
K86A / K87A / K88A Cc
C
NPM1
DIC
WT Cc
K5A / K7A / K8A Cc
K86A / K87A / K88A Cc
D
1:5 molar ratio
1:10 molar ratio
Area occupancy (%)
WT Cc
K5A / K7A / K8A Cc
K86A / K87A / K88A Cc

Figure 4. Effects of Lys-to-Ala substitutions of cytochrome *c* on its ability to phase-separate with SET/TAF-Iβ and NPM1

(A) Fluorescence and DIC microscopy images of condensates driven by 10 μM SET/TAF-Iβ with 160 μM WT, K5A/K7A/K8A or K86A/K87A/K88A C*c* variants (1:16 molar ratio). SET/TAF-Iβ was used as 90% unlabeled SET/TAF-Iβ and 10% SET/TAF-Iβ Q69C mutant labeled with Oregon Green 488 (green). Scale bars: 30 μm.

(B) Percentage of area in the microscopy field occupied by protein condensates as a function of both the chaperone:C*c* molar ratio (10 μM SET/TAF-Iβ) and NaCl concentration. WT, K5A/K7A/K8A and K86A/K87A/K88A C*c* variants are at the *upper*, *middle*, and *lower* histograms, respectively. Error bars represent the standard deviation (SD) calculated from 10 images per each protein complex.

(C) Fluorescence and DIC microscopy images of condensates driven by 10 μM NPM1 with 50 μM WT, K5A/K7A/K8A or K86A/K87A/K88A C*c* variants (1:5 molar ratio). NPM1 was used as 10% labeled with Oregon Green 488 (green). Scale bars: 30 μm.

(D) Percentage of area in the microscopy field occupied by protein condensates as a function of chaperone:C*c* molar ratio with 10 μM NPM1 at 100 mM NaCl. Error bars represent the SD from 10 images per each protein complex.

dimeric SET/TAF-Iβ,[43] sampling the "earmuff" interfaces and the C-end tails of the chaperone. Then, SET/TAF-Iβ:C*c* phase co-separation requires partial charge compensation of the anionic disordered tail of SET/TAF-Iβ, although still leaving unsatisfied valences (i.e., charged amino acids or patches that are available for interaction) to maintain droplet fluidity.[66] The inability of SET/TAF-Iβ or C*c* to phase separate alone—even in the presence of crowding agents, such as Ficoll[67] (Figure S3)—confirms that the interaction between the two proteins triggers condensate assembly.

SET/TAF-Iβ is a histone chaperone that exhibits a strong negative electrostatic potential surface that hinders protein PS via homotypic interactions (Figures 3B and S1). However, the C-end Asp/Glu-rich IDRs of SET/TAF-Iβ, which bind to C*c*[43,44] and show multivalent nature, may contribute to heterotypic contacts with C*c* and, therefore, liquid condensate formation. Actually, titrating a SET/TAF-Iβ construct lacking its C-end IDRs (SET/TAF-Iβ ΔC) with C*c* resulted in liquid droplets only at very high SET/TAF-Iβ ΔC:C*c* molar ratios (1:24, Figures 3C and S4). This finding reveals the paramount importance of the disordered, negatively charged C-tails of SET/TAF-Iβ in its C*c*-mediated PS (Figures 3C and S4).

SET/TAF-Iβ:C*c* enriched droplets are sensitive to NaCl (100 mM), thus confirming their electrostatic nature (Figure S4C). Complete abolition of liquid-like droplets occurred in the presence of SET/TAF-Iβ ΔC and C*c* at 100 mM NaCl (Figure S4C). This is consistent with our former results on the breaking off of the SET/TAF-Iβ ΔC:C*c* complex with high ionic strength, but not the SET/TAF-Iβ:C*c* ensemble.[43,44] This finding confirms that the disordered, multivalent and anionic C-end tails of SET/TAF-Iβ act as scaffolding units of the electrostatic droplet network together with C*c*.

K-blocks of cytochrome *c* prompt phase co-separation with histone chaperones

To explore whether Lys-based stickers of C*c* are responsible for PS together with its nuclear targets SET/TAF-Iβ or NPM1, the two N-end or C-end K-blocks were mutated by Ala residues (Figures S5 and S6). Both histone chaperones were titrated with wild-type (WT), K5A/K7A/K8A or K86A/K87A/K88A C*c* variants, to monitor droplet growth and quantify them under different ionic strength conditions (Figure 4).

The removal of C*c* K-blocks substantially decreased the number of condensates in the presence of SET/TAF-Iβ or NPM1, being almost absent in those assays that include the K5A/K7A/K8A C*c* mutant (Figure 4). In the presence of K86A/K87A/K88A C*c* mutant, a slight increase of PS was observed for chaperone:C*c* molar ratios up to 1:16 and 1:24 with SET/TAF-Iβ and 1:10 with NPM1. However, these biomolecular condensates show irregular shapes that more closely resemble solid-like aggregates than liquid phase-separated bodies.

Condensates harboring triple Lys-to-Ala C*c* mutants, along with SET/TAF-Iβ, were still sensitive to ionic strength despite having neutralized three positive charges each, as their size and abundance decreased in a NaCl-concentration dependent manner (from 50 to 100 mM NaCl, Figure 4B). This suggests that (I) both N-end and C-end K-blocks are necessary for droplet assembly in agreement with reported nuclear magnetic resonance (NMR) data[34,43] (Figures 2B and 2C); and (II) they are not sufficient and other lysine residues scattered on C*c* surface may be involved in binding and PS with SET/TAF-Iβ. For liquid droplets involving NPM1, a fixed ionic strength (100 mM NaCl) was kept in all experiments to ensure, on one hand, the stability and consequent functionality of the NPM1 pentamer[55] and, on the other hand, experimental conditions to guarantee that NPM1 phase separates[56] (Figure 4D).

Consistently, triple Lys-to-Ala C*c* mutants have a significant impact in complex formation with SET/TAF-Iβ and NPM1, as inferred from isothermal titration calorimetry (ITC) (Table 1; Figure S7). In particular, the binding affinity of complexes between SET/TAF-Iβ and K5A/K7A/K8A or K86A/K87A/K88A C*c* mutants decreased in an order of magnitude with respect to those with WT C*c*, followed by a drastic reduction in cooperativity between the two binding sites for C*c* on SET/TAF-Iβ surface. Such synergy was completely abolished in ensembles involving the triple C-end Lys-to-Ala C*c* mutant, where the two-binding events became independent and enthalpically driven (Table 1). On the other hand, the thermodynamic profile of the interaction between K5A/K7A/K8A C*c* and SET/TAF-Iβ is entropically driven, as occurs for WT C*c*. Such thermodynamic behavior is characteristic of electrostatically guided adducts, due to the entropy increase caused by the exclusion of water molecules surrounding charged, interacting protein interfaces (see Note S1). On the contrary, the global thermodynamic endothermic-to-exothermic shift observed for the interaction involving K86A/K87A/K88A C*c* is consistent with a significant reduction of the aforementioned desolvation—mainly due to the displacement of water molecules away from molecular interface—coupled to attenuated electrostatics. This is in agreement with the change in the electrostatic surface potential (ESP) of C*c* induced by the K86A/K87A/K88A mutation, whose attenuation is more prominent than that of K5A/K7A/K8A C*c* (Figure S8). Moreover, the triple C-end Lys-to-Ala substitution may promote additional hydrophobic interactions between C*c* molecules, since the resulting K86A/K87A/K88A stretch would be surrounded by other hydrophobic residues already present in WT C*c*.

Table 1. Thermodynamic parameters of SET/TAF-Iβ in complex with cytochrome *c* variants.

Protein complex	K_D (μM)	Δ*G* (kcal/mol)	Δ*H* (kcal/mol)	-TΔ*S* (kcal/mol)	n	ρ
WT Cc : SET/TAF-Iβ	3.6	−7.43	1.30	−8.73	1.2	1.24
K5A/K7A/K8A Cc : SET/TAF- Iβ	45.5	−5.92	5.70	−11.62	0.9	0.52
K5R/K7R/K8R Cc : SET/TAF- Iβ	2.0	−7.77	−15.00	7.23	1.1	0.76
K86A/K87A/K88A Cc : SET/TAF- Iβ	40.0	−6.00	−6.10	0.10	2.3[a]	N/A
K86R/K87R/K88R Cc : SET/TAF- Iβ	5.9	−7.13	−7.70	0.57	1.1	0.80

Calculated equilibrium intrinsic dissociation constants (K_D), Gibbs free energy (Δ*G*), association enthalpy (Δ*H*), entropic term (-TΔ*S*), active protein fraction (n) and cooperativity factor (ρ) are displayed for SET/TAF-Iβ reactions with WT or Lys-mutated Cc variants. Relative errors are less than 20% for K_D and 10% for Δ*H*. These values are provided by the fit to a two cooperative-binding sites model for complexes involving WT, K5A/K7A/K8A, K5R/K7R/K8R and K86R/K87R/K88R Cc, or to a set of identical and independent binding sites model for the K86A/K87A/K88A Cc:SET/TAF-Iβ complex.
N/A, Not applicable.
[a]n stands for the binding stoichiometry in the K86A/K87A/K88A Cc:SET/TAF-Iβ complex, with independent binding sites.

Binding effects of triple Lys-to-Ala Cc mutants complexed with NPM1 were more pronounced. While the K_D increased two orders of magnitude (from 6.5 to 300 μM) in the complex with the K86A/K87A/K88A Cc mutant, no interaction was detected between K5A/K7A/K8A Cc and NPM1 (Table 2; Figure S7).

Altogether, both N-end and C-end K-blocks are hallmarks of multivalency in Cc that regulate its electrostatic coacervation in complex with SET/TAF-Iβ or NPM1.

Molecular grammar of cytochrome *c*-containing condensates: the role of K-blocks versus and R-blocks

Despite the general, classical debate that lysine and arginine residues operate similarly within proteins—due to their status as basic amino acids—many works have evidenced that their divergent chemical characteristics make them different in terms of binding and multivalency.[68,69] As a consequence, they specifically drive different location and functional propensities to the proteins by modifying their PS ability.[19,70] To reveal molecular mechanisms that lead Cc K-blocks to phase separate with SET/TAF-Iβ or NPM1, triple Lys-to-Arg Cc mutants were designed (Figures S5 and S6).

Replacing Lys5, Lys7, and Lys8 of Cc by Arg residues resulted in an increase of quantity and size of condensates—with respect to WT Cc—with either SET/TAF-Iβ or NPM1 (Figure 5). Droplets containing SET/TAF-Iβ and K5R/K7R/K8R Cc remain dependent on ionic strength (Figure 5B). However, mutations of Lys86, Lys87 and Lys88 from Cc by Arg almost abolished the condensation process, especially in the presence of NPM1. Indeed, the occupied areas by droplets decreased ca. 10-fold at all molar ratios (Figure 5).

Despite drastic consequences that triple Lys-to-Arg Cc mutants performed in conducting PS with SET/TAF-Iβ or NPM1, slight differences in binding affinities were determined between Arg-mutants or WT Cc with both chaperones. Their thermodynamic profiles revealed, however, remarkable disparities in recognition modes that could be underlying prominent changes in their PS, especially those harboring SET/TAF-Iβ. ITC measurements showed that the SET/TAF-Iβ-binding process of both Arg-Cc variants is enthalpically driven ($\Delta H < 0$; $-T\Delta S > 0$), contrary to what is found in that for WT Cc (Table 1; Figure S7), and typically in complexes involving IDRs, electrostatic-based ensembles and then coacervation-mediated LLPS events.[71–74] Such enthalpically driven thermodynamic profile has been ascribed to the formation of weak interactions—such as H-bonds or van der Waals forces[71]—involved in intermolecular recognition (see Note S1). The deconvolution of the thermodynamic parameters of the SET/TAF-Iβ complexes with different Cc variants rendered separately the values for the first interaction event and that affected by cooperativity (Table S1). Whereas the first molecular-recognition event followed the aforementioned thermodynamic behavior (governed by enthalpy; $\Delta H < 0$ and $-T\Delta S > 0$), the binding step governed by cooperativity became entropically driven ($\Delta H > 0$; $-T\Delta S < 0$).

Table 2. Thermodynamic parameters of NPM1 in complex with cytochrome *c* variants.

Protein complex	K_D (μM)	Δ*G* (kcal/mol)	Δ*H* (kcal/mol)	-TΔ*S* (kcal/mol)	n
WT Cc : NPM1	6.5	−7.06	0.6	−7.66	1.9
K5A/K7A/K8A Cc : NPM1			No interaction		
K5R/K7R/K8R Cc : NPM1	14.0	−6.61	0.60	−7.21	2.0
K86A/K87A/K88A Cc : NPM1	300.0	−4.81	7.20	−12.01	2.0
K86R/K87R/K88R Cc : NPM1	15.0	−6.57	2.30	−8.87	1.8

Calculated equilibrium dissociation constants (K_D), Gibbs free energy (ΔG), association enthalpy (Δ*H*), entropic term (-TΔ*S*), and reaction stoichiometry (n) are displayed for NPM1 reactions with WT or its Lys-mutated Cc variants. Relative errors are less than 20% for K_D and 10% for Δ*H*. These values are provided by the fitting to a set of identical and independent binding sites model.

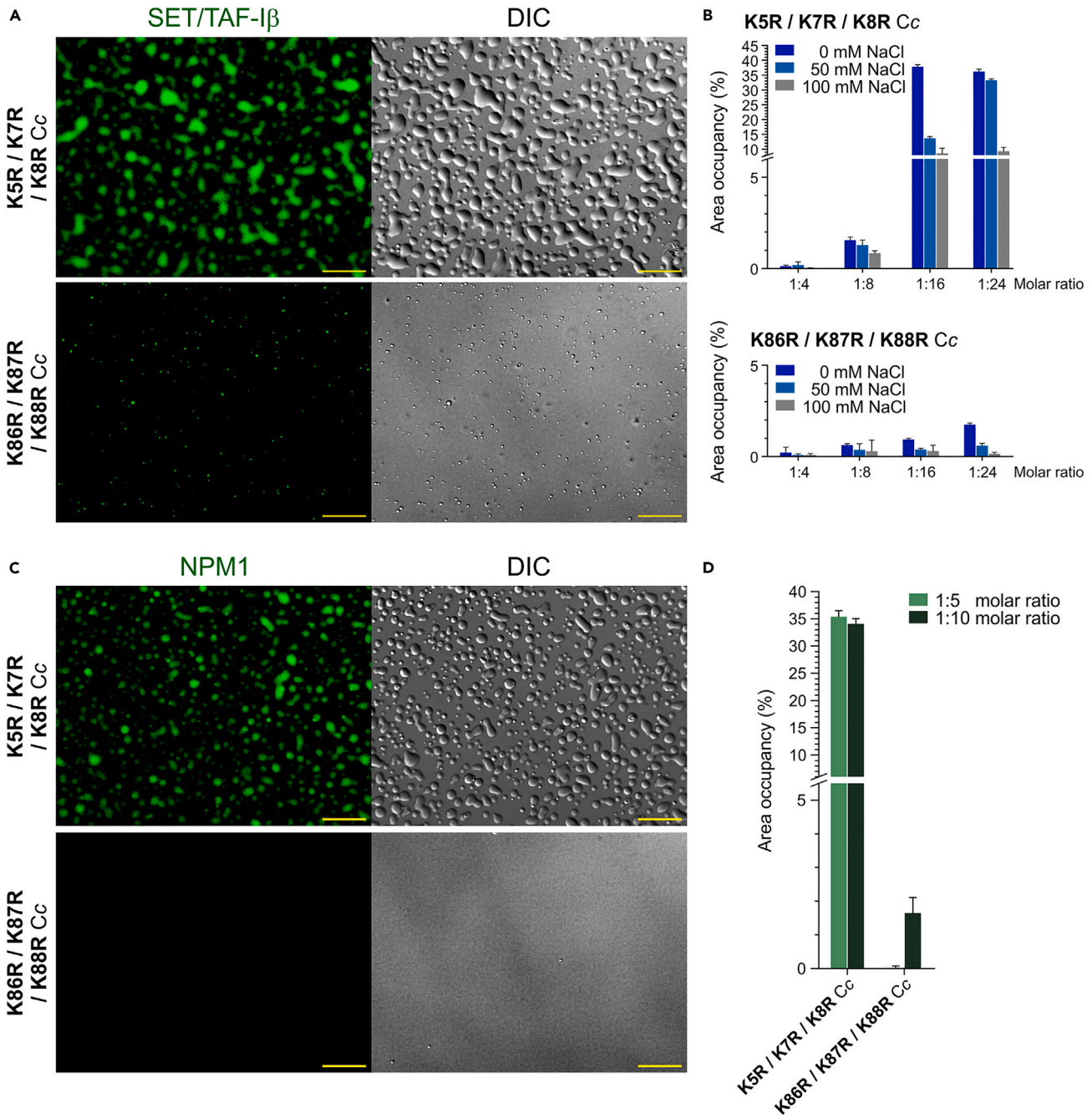

Figure 5. Effects of Lys-to-Arg substitutions of cytochrome *c* on its ability to phase-separate with SET/TAF-Iβ and NPM1

(A) Fluorescence and DIC microscopy images of condensates driven by 10 μM SET/TAF-Iβ with 160 μM K5R/K7R/K8R or K86R/K87R/K88R C*c* variants (1:16 molar ratio). SET/TAF-Iβ was used as 90% unlabeled SET/TAF-Iβ and 10% SET/TAF-Iβ Q69C mutant labeled with Oregon Green 488 (green). Scale bars: 30 μm.

(B) Percentage of area in the microscopy field occupied by protein condensates as a function of both the chaperone:C*c* molar ratio (10 μM SET/TAF-Iβ) and NaCl concentration. Error bars represent the standard deviation (SD) calculated from 10 images per each protein complex.

(C) Fluorescence and DIC microscopy images of condensates driven by 10 μM NPM1 with 50 μM K5R/K7R/K8R or K86R/K87R/K88R C*c* variants (1:5 molar ratio). NPM1 was used as 10% labeled with Oregon Green 488 (green). Scale bars: 30 μm.

(D) Percentage of area in the microscopy field occupied by protein condensates as a function of chaperone:C*c* molar ratio with 10 μM NPM1 at 100 mM NaCl. Error bars represent the SD from 10 images per each protein complex.

To explain the inversion of the thermodynamic profile for the first binding event upon replacement of Lys blocks by Arg, we further analyzed the intramolecular H-bonds during molecular dynamics (MD) computed on Arg-variants. Indeed, Arg sidechains established additional intramolecular H-bonds in the two K5R/K7R/K8R and K86R/K87R/K88R C*c* mutants (Figure S9A), although the total number of H-bonds involving all potential donor/acceptor atoms of C*c* remains constant when mutants are compared with WT C*c* (Figure S9B). Such an apparent compensation of the new H-bonds rising in C*c* Arg-mutants with respect to the WT lead to maintain the overall folding of the hemeprotein. In particular, Arg5 is able to form largely represented H-bonds with sidechains of Glu89 and Asp93, which are located at the C*c* helix 4 (Figure S9C). These weak H-bond contacts probably limit the mobility of helix 4 with respect to helix 1 and, therefore, hinder the plasticity and dynamics of such motifs to recognize SET/TAF-Iβ. Similarly, Arg7 and Arg87 establish H-bonds with sidechains of acidic residues respectively placed at a distance of one helix turn, contributing to helix stability (Figure S9C). Detailed data of H-bonds analyses on the different C*c* variants are given in Table S2. To make these sidechains available to chaperones, the disruption of the aforementioned intramolecular contacts is first required. Thus, the heat release observed for the first binding event ($\Delta H < 0$; Table S1) would respond to the formation of energetically favorable interactions—either H-bonds or cation-π—established by non-H-bonding Arg residues in C*c* with acceptor residues of SET/TAF-Iβ. This may explain the global endothermic-to-exothermic transition profile ($\Delta H < 0$; $-T\Delta S > 0$) showed by C*c* Arg-mutants-dependent complexes. This phenomenon is more pronounced for ensembles with K5R/K7R/K8R C*c*, in agreement with the larger number and frequency of H-bonds formed by Arg sidechains and also the substantial NMR CSPs experienced by residues 5 and 7, *vis-à-vis* residue 87, in complex with SET/TAF-Iβ (Figures 2B and 2C).

Interestingly, the cooperativity makes the second binding event entropically driven ($\Delta H > 0$ and $-T\Delta S < 0$; Table S1), revealing multivalent recognition between positively charged R-blocks from C*c* and anionic unstructured C-tails of SET/TAF-Iβ that lead to the paradoxical disorder-to-order transition in droplets.[75,76] The release of water molecules from binding interfaces during PS may also contribute to a favorable entropy[74] (see Note S1). The molecular reorganization of SET/TAF-Iβ was further confirmed by site-directed spin labeling electron paramagnetic resonance (SDSL-EPR). Four single-Cys mutants on residues distributed along the SET/TAF-Iβ IDRs—namely D226C, E243C, D260C, and D277C—were designed and used for spin labeling by MTSL. Continuous wave (CW) X-band EPR spectra of each spin-labeled variant of SET/TAF-Iβ were recorded at room temperature, for the protein both alone (80 μM) and in complex with C*c* (1:2 molar ratio). EPR spectra of SET/TAF-Iβ alone showed narrow lines indicative of high flexibility, due to the intrinsically disordered nature of these domains. This flexibility was restricted for the D226C^{MTSL} species when compared to the three other positions, showing some structural constraints consistent with its location near the globular earmuff domains (Figure S10). When C*c* was added, the spectrum broadened for position 226, reflecting a decrease in label mobility. A slight broadening was also observed for positions 243 and 260, indicating a local loss of mobility for those residues placed at the central positions of the IDR. This indicates that the dynamics of the middle IDR of SET/TAF-Iβ is restricted upon C*c* binding (Figure S10), in agreement with IDRs dynamics into condensates.[77] Within this frame, thermodynamic profiles inferred from the interaction of Arg-C*c* variants on two independent binding sites on NPM1 surface are also entropically driven (Table 2; Figure S7).

Changes in the ESPs of C*c* upon Lys-by-Arg mutations (Figure S8) can modulate the binding mode and PS properties of the hemeprotein with SET/TAF-Iβ and NPM1. In addition, both Arg-mutants exhibited an increased global dynamics, with the stretch comprising residues 20–65 being particularly mobile (Figure S11), although the overall secondary structures remained unaltered, as inferred from far-UV circular dichroism (CD) spectra (Figure S12) and MD trajectories (Figure S13). For K86R/K87R/K88R C*c* variant, its heme environment was slightly perturbed, as demonstrated by NMR chemical-shifts of the Met80-εCH_3 resonance (ca. −3.36 ppm due to its chemical environment[43,78]), corresponding to an axial ligand of ferrous heme iron (Figure S14). However, the Cotton effect at the Soret-band absorption wavelength[79]—monitored by visible-CD spectroscopy—suggested that the heme coordination of oxidized C*c* variants did not change (Figure S15A). Substantial changes in the midpoint redox potential values of the C*c* variants were also not expected as they were completely oxidized or reduced upon addition of sodium ferricyanide or ascorbate, respectively, as observed for most of *c*-type cytochromes[80,81] (Figure S15B). These subtle changes in the heme moiety upon replacement of the C-terminal K-block by Arg, probably due to long-range dynamics effects, alter the heme-surrounding binding interfaces—important for SET/TAF-Iβ or NPM1 binding[34,43]—and explain the decrease in PS involving this triple C*c* mutant.

Despite Arg and Lys residues being both positively charged at physiological pH,[82] the guanidium group planarity contributes to delocalize the electron cloud and to form H-bonds with perfect colinear angles.[69,83] In MD calculations, the guanidium moiety shows more propensity than amine groups to form H-bonds with negatively charged residues at helices 1 and 4 in C*c*. The arginines, along with their tendency of forming H-bonds, neutralize part of the positive potential on the hemeprotein surface, in particular the area surrounding positions 86-87-88 (Figure S9). In turn, this slightly weakens the binding of K86R/K87R/K88R C*c* to SET/TAF-Iβ and NPM1 (Tables 1 and 2). Indeed, previous studies revealed that Lys87 and Lys88 of C*c* underwent large CSPs upon NPM1 binding[34,43,44] (Figures 2B and 2C).

In other words, a K-block-based molecular grammar governs the driving forces for binding and PS of C*c* with its nuclear targets SET/TAF-Iβ and NPM1.

Selective cytochrome *c*-mobility inside electrostatic coacervates harboring SET/TAF-Iβ or NPM1

To further explore the PS experienced by SET/TAF-Iβ and NPM1 with C*c* or its Arg-mutants, the dynamics of the proteins inside condensates have been characterized in order to determine any potential correlation between such dynamics and the binding characteristics of these protein complexes. Mobility of protein components inside condensates was followed by fluorescence recovery after photobleaching (FRAP) assays on droplets with Oregon Green 488-labeled SET/TAF-Iβ or NPM1 and Texas Red-labeled C*c* variants—all of them 10% labeled—in a 1:16 (SET/TAF-Iβ:C*c*) o 1:10 (NPM1:C*c*) molar ratios.

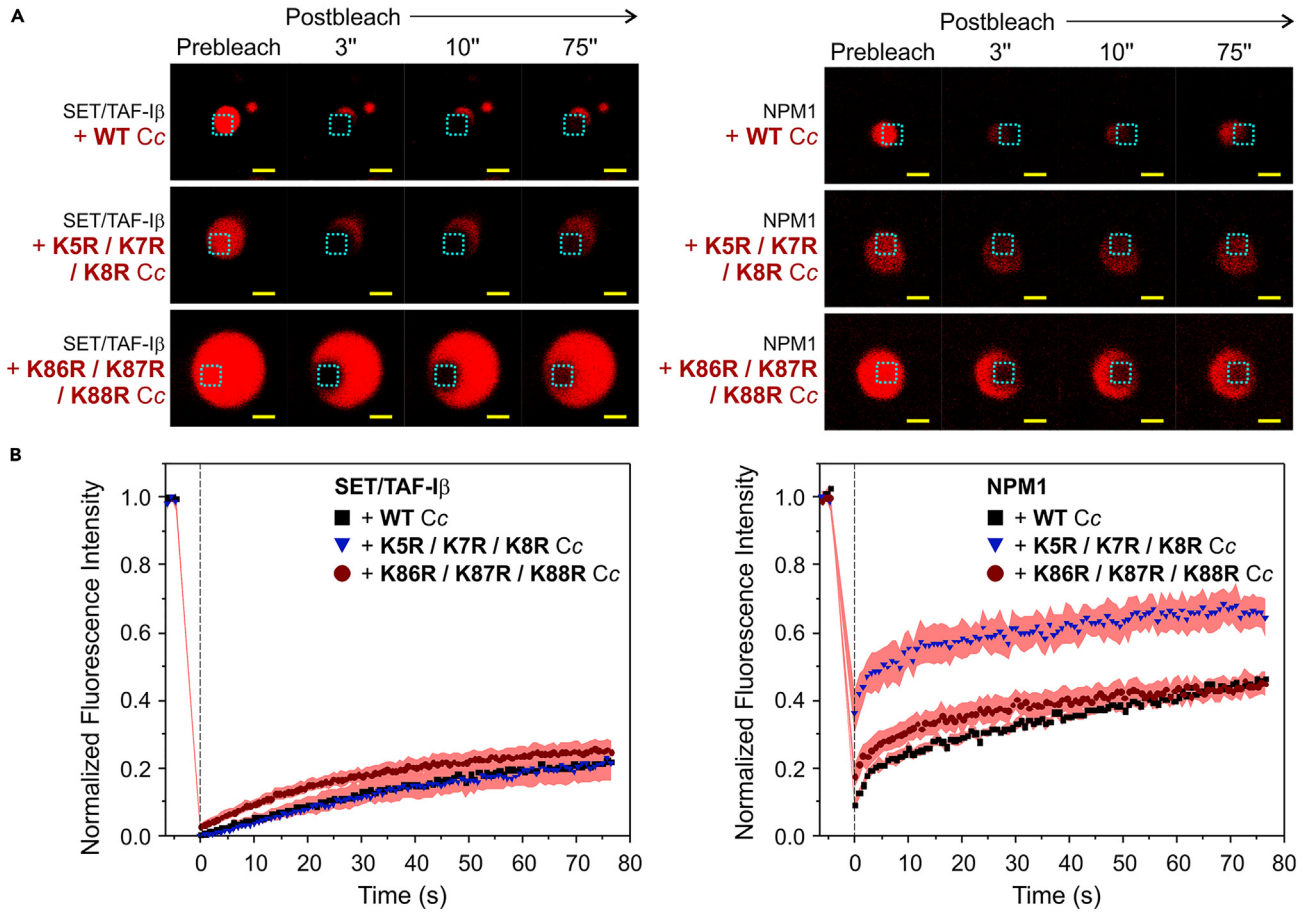

Figure 6. FRAP measurements on droplets assembled by cytochrome *c* variants with SET/TAF-Iβ or NPM1

(A) Fluorescence recovery of ROIs (cyan dashed squares) from droplets containing fluorescent labeled WT, K5R/K7R/K8R or K86R/K87R/K88R Cc variants in complex with SET/TAF-Iβ (*left panel*) or NPM1 (*right panel*). Confocal microscopy images are shown before bleaching (prebleach) and 3, 10, and 75 s postbleaching. Scale bars: 1 μm.

(B) Kinetics of labeled Cc fluorescence emitted from the bleached regions of droplets containing SET/TAF-Iβ (*left panel*) or NPM1 (*right panel*), after background subtraction and normalization of intensities. Coral shadows represent the standard error of the mean (SEM) for 4 or 5 droplets per protein complex.

Droplets containing SET/TAF-Iβ showed low fluorescence recovery of the WT, K5R/K7R/K8R and K86R/K87R/K88R Cc variants, with average mobile Cc fractions between 21 and 23% (Figure 6A; Table S3). These FRAP profiles and time-course curves are consistent with mature PS systems rather than highly fluid liquid droplets,[84,85] whose rheological properties seem to agree with gelation or percolation processes.[86,87] Percolation events would be induced by a compact electrostatic network built between SET/TAF-Iβ scaffolds and Cc variants, and intimately imbricated by the addition of new intermolecular, multivalent contacts along with the entropically driven conformational rearrangement of SET/TAF-Iβ IDRs, as suggested by thermodynamics and EPR assays.[77,88] It is worth noting that K86R/K87R/K88R Cc exhibited a faster recovery kinetics (average half-recovery time [$t_{1/2}$], 21.3 s), than WT and K5R/K7R/K8R Cc ($t_{1/2}$, 47.8 and 42.4 s, respectively) (Table S3), likely related to larger K_D/ρ values (Table S1), which in turn relates to fewer and smaller condensates (Figure 5A).

NPM1-harboring condensates clearly showed liquid-like behavior, with fluorescence recovery rates ranging from 32% to 47% for different Cc variants[85,89] (Figure 6B; Table S4). The apparent enhanced mobility of K5R/K7R/K8R Cc variant could be explained by the subordinate role played by the N-terminal Lys cluster of Cc—in comparison with the C-end Lys stretch—in LLPS with NPM1 (Figure 5B). In this case, the fluorescence-recovery rate for both Lys-to-Arg Cc mutants was significantly faster than that of the WT. Then, like complexes involving SET/TAF-Iβ, there is an inverse relationship between $t_{1/2}$ values of Cc variants from FRAP assays and the K_D values of their adducts with NPM1 (Table 2).

When fluorescence recovery from labeled SET/TAF-Iβ or NPM1 was monitored by FRAP assays performed within the same condensates that were previously analyzed for Cc, the mobility that both chaperones exhibited was negligible (Figure S16; Tables S3 and S4). The high Cc concentration to induce coacervate assembly contributes to saturate the pool of chaperone molecules, limiting their mobility inside droplets and their exchange with the diluted phase. The slightly higher mobility observed for both chaperones when phase-separated with WT Cc (Tables S3 and S4) might be explained by a higher contribution of complex coacervation to their PS compared to that with Cc Arg-mutants.

DISCUSSION

In the last years, LLPS has emerged as a fundamental biophysical mechanism underlying a wide variety of biological processes that need to be spatial-temporally delimited from the general subcellular bulk. In particular, a wide variety of nuclear proteins and complexes and their functionalities have been reported to be relevant when delineated within condensates, either as organelle-entities or transient bodies, such as nucleoli, nuclear speckles and paraspeckles, Cajal bodies, histone-locus bodies, chromatin domains or condensates mediating transcription, DNA replication or repair.[17,90] Among them, the processing of chromatin both under homeostatic—e.g., for heterochromatin assembly or transcription—or stress conditions—DNA damage signaling and repair—requires the compartmentalization or exclusion by LLPS of a wide multitude of effectors on DNA segments. Specifically, DNA damage responses utilize a tightly orchestrated network of phase-separating proteins, nucleic acids and the DNA damage-induced polymer poly(ADP-ribose) (PAR) to control genome integrity in a highly specific manner.[17] PARs are formed locally at DNA-damage sites and recruit a plethora of PAR-binding proteins—most of them being intrinsically disordered and establish multivalent electrostatic interactions—to cluster the damaged DNA[91] and the subsequent foci and repair effectors.[65,92] Within this framework, the oncoprotein SET/TAF-Iβ stands out as an IDR-containing chromatin remodeller[39] capable of counteracting DNA repair in DNA foci.[41]

Here we report for the first time the ability of SET/TAF-Iβ to undergo PS upon binding to C*c*, which translocates to the nucleus soon after DNA damage and counteracts the function of the histone chaperone in several manners.[43,44] In this context, we find that the acidic disordered C-tails of SET/TAF-Iβ—which are also essential for the recognition of histones—play a capital role in PS by powering the multivalency of SET/TAF-Iβ. Then, the ability of C*c* to form LLPS with SET/TAF-Iβ offers a potential mechanism for C*c* to be incorporated into DNA damage repair foci and interfere with the SET/TAF-Iβ function. Similarly, the involvement of LLPS processes in nucleosome assembly involving SET/TAF-Iβ and even C*c*, cannot be ruled out at all.

Within this framework, we have investigated the molecular mechanisms used by C*c* to phase-separate with SET/TAF-Iβ and with its previously described phase-separating partner NPM1. Building on previous evidence, we find that Lys residues scattered in clusters on C*c* surface mainly mediate binding and PS with both partners, being the holders of its multivalency. In particular, two triple-Lys patches, placed at both its N-end and C-end helices, act as essential PS stickers in uneven manners by virtue of their chemical nature, orientation and structural dynamics. Observing the effect derived from the replacement of K-blocks allowed us to discriminate the different functions accomplished by them as powerful stickers in C*c*. While the N-end K-block is directly involved in protein recognition contacts, the C-end one is responsible for the dynamical rearrangement of SET/TAF-Iβ that allows the cooperative and multivalent recognition of the hemeprotein and then, their PS. It is plausible that such a dynamical rearrangement would involve the transition from allovalent—as observed for other charged intrinsically disordered proteins containing repetitive sequence features[93]—to multivalent recognition of C*c* by the SET/TAF-Iβ IDRs. Binding cooperativity then leads to the entropy gain, which is characteristic of electrostatic-based multivalent IDR-involving complexes[75,76] and to the water exclusion that occurs upon condensation[74] (see Note S1). A simpler thermodynamic landscape was described by NPM1-mediated complexes together with C*c* variants. Two independent binding sites on NPM1 are recognized by C*c*, with a significant entropy gain upon complex formation. This is consistent with the multivalency of NPM1 and its ability to phase separate by itself—as widely demonstrated by other works[54,56]—without the need for another partner to induce dynamical rearrangements in the binding and subsequent condensation. To sum up, we suggest that the N-end and C-end K-blocks of C*c* act as primary stickers from which the droplet network harboring histone chaperones is built. In the case of SET/TAF-Iβ, the recognition of the C-end cluster drives the dynamical rearrangement of the chaperone that allows its phase transition.

Interestingly, phase separation of SET/TAF-Iβ requires C*c* binding just to compensate the remarkable negative ESP of the chaperone. A similar behavior may be shown by the acidic Leu-rich nuclear phosphoprotein 32 (ANP32) family members A and B, being unable to phase separate under molecular crowding conditions (unpublished data). Like SET/TAF-Iβ, ANP32A and ANP32B are also nuclear targets of C*c* that lack positive R/K-tracts and have acidic, D/E-rich IDRs whose repulsion would minimize homotypic contacts. The shielding of IDRs negative charges by C*c*, which induces molecular reorganization,[94] might also underlie a possible phase separation experienced by this type of chaperones.

Replacing the Lys residues of C*c* by Arg provided more details about the specific roles played by both K-blocks. Being also a positively charged residue at physiological pH due to its high pK_a,[82] primary electrostatics does not make the difference between Lys and Arg. However, both residues exhibit very different chemical properties that make them truly distinct as drivers of PS.[68–70] First, the planarity of the guanidinium group causes the electron cloud of ionized Arg to be delocalized, conferring it "Y-aromaticity" and a directional preference to form cation-π interactions with aromatic—Tyr and Phe—residues, in contrast to Lys.[68,83] In addition, their ability to form H-bonds is also substantially different. Arg-guanidinium possesses more atoms capable of forming H-bonds—as reflected by the emergence of local H-bonds when Arg is present—and does so with almost perfectly colinear angles. In contrast, despite being less sterically constrained, Lys is only able to form one H-bond with optimal orientation, as the formation of more than one is accompanied by angle distortions. For these reasons, Arg is expected to establish stronger interactions within condensates.[70] Thus, ITC analyses of complexes between C*c* Arg-mutants and SET/TAF-Iβ exhibited thermodynamics consistent with the breakage and replacement of intramolecular interactions established by Arg residues—reflected by MD—by the onset of new intermolecular ones. Moreover, Arg at the N-end of C*c* led to the greater formation of condensates with both SET/TAF-Iβ and NPM1. Given the role of this Lys patch in direct interaction with both chaperones, such effect is explained by the greater ability of Arg to establish more H-bonds and strong cation-π interactions with Tyr sidechains.[95] Substitution of the C-end Lys cluster by Arg did not compromise the effect of cooperativity in the SET/TAF-Iβ recognition, but strongly abolished condensate formation with both SET/TAF-Iβ and NPM1. We found that substitution of this Lys patch led to long-range changes in the dynamics of C*c* that affected the heme surroundings. The C-end K-block is included, along with other Lys that are closer to the heme cleft, in the interacting

surface that Cc uses to recognize both histone chaperones.[34,43] It is then likely that the C-terminal Lys patch acts not only as a sticker but also as a spacer, by controlling the appropriate orientation of other putative stickers distributed across the Cc surface.

On another level, we observed differences in the dynamics of the condensates formed by Cc with SET/TAF-Iβ or NPM1. We observed that Cc exhibited lower turnover in condensates formed by SET/TAF-Iβ than in those assembled by NPM1. The faster Cc dynamics into NPM1-containing condensates is in agreement with that of molecules incorporating to scaffold-stablished condensates in the cell.[51] This is consistent with the ability of NPM1 to phase separate with itself and scaffold the nucleoli. Indeed, the exchange of NPM1-associated factors between nucleoli and nucleoplasm, including Cc, is well documented.[34,51] In contrast, SET/TAF-Iβ:Cc condensates exhibit low dynamics. Such a reduced turnover of protein molecules is probably due to the coupling of gelation or percolation processes.[96] The maturation of LLPS into solid- or gel-like condensates has been observed as a part of both normal and pathological biological responses.[30] Some of these rheological evolutions act reversibly to regulate cellular responses by constraining or loosening protein dynamics within such condensates.[97,98] Indeed, an example is that of HP1α, whose phase-separating dynamics fluctuations directly modulates the dynamics of heterochromatin.[49] Altogether, it is tempting to propose that the role of SET/TAF-Iβ within DNA foci would be precisely to decrease their dynamics by itself—since it consists on arrest proteins at DNA breaks[41]—or by incorporation of Cc. In support of this hypothesis, Cc has recently been shown to increase the residence time of SET/TAF-Iβ on nucleosomes, thereby slowing-down its turnover in the context of histone eviction and deposition.[99] In this context, it has been previously proposed that the concentration of Cc reaching the nucleus may be variable and dependent on the level of DNA damage.[100] Since high stoichiometric amounts of Cc are required for PS with SET/TAF-Iβ, it could be suggested that, under exacerbated DNA damage, PS provides a molecular mechanism involving retention of chaperones in nucleosomes and blockage of repair of DNA.

In summary, we report here the case of a small and globular protein with sequence-encoded heterotypic PS properties. Such condensation capability is primarily determined by Lys clusters distributed on its surface, which confers multivalency. In addition, Cc represents a paradigm of an evolutionarily selected mechanism to perform PS, both by virtue of its thermodynamic way to recognize its phase-separating partners and its control of the intrinsic dynamics of the molecule. Furthermore, Lys expands the regulatory span through protein post-translational modification (PTM), since it is a substrate for many more types of PTMs than Arg and has been found to be modified more frequently along the proteome.[101] In fact, in the particular case of Cc, different Lys acetylation and methylation have been detected affecting mitochondrial electron transfer in different pathological contexts.[102–104] Lysine succinylation of Cc has also been reported, although specific functional effects of this PTM have not been further investigated.[105] In the context of PS, PTMs are being increasingly documented as a mechanism by which multivalency of proteins PS is modified.[17,106] Thus, a possible relevance of Lys-PTMs over its LLPS ability and derived functions cannot be excluded.

Limitations of the study

The main goal of this study is to unveil the molecular mechanisms underlying protein phase separation *in vitro* using a biophysical approach. In particular, the article focusses on those processes that govern the condensation of Cc together with its nuclear targets under stress conditions. Whereas Cc undergoes phase separation towards the nucleolus by binding to NPM1 to modulate the cellular DDR, further studies will be necessary to explore the co-phase separation of Cc and SET/TAF-Iβ *in vivo* and its biological relevance.

STAR★METHODS

Detailed methods are provided in the online version of this paper and include the following:

- KEY RESOURCES TABLE
- RESOURCE AVAILABILITY
  - Lead contact
  - Materials availability
  - Data and code availability
- METHOD DETAILS
  - DNA constructs
  - Protein expression and purification
  - Circular dichroism spectroscopy
  - Mass spectrometry
  - Protein spin labeling
  - Electron paramagnetic resonance
  - Nuclear magnetic resonance
  - Molecular dynamics computations
  - Electrostatic surface potential computations
  - Isothermal titration calorimetry
  - Protein fluorescent labeling
  - Phase separation assays and imaging
  - Fluorescence recovery after photobleaching
- QUANTIFICATION AND STATISTICAL ANALYSIS

- Phase separation assays
- Fluorescence recovery after photobleaching
- Molecular dynamics: H-bonds calculations

SUPPLEMENTAL INFORMATION

Supplemental information can be found online at https://doi.org/10.1016/j.isci.2024.110435.

ACKNOWLEDGMENTS

This work was supported by the Agencia Estatal de Investigación (AEI), the Spanish Ministry of Science and Innovation (MCIN) and "ERDF A way of making Europe" (MCIN/AEI/10.13039/501100011033, grant number PID2021-126663NB-I00); the European Regional Development Fund (FEDER); the Andalusian Government (BIO-198); the University of Seville (VI PPIT) and the Ramón Areces Foundation. This work was also supported by Ministry of Education and Professional Training (FPU18/06577 for M.A.C.-C.), Biointeractomics Platform (cicCartuja, Seville) and the NMR Services at CITIUS (University of Seville). The APC for open-access publication was funded by the University of Seville. For EPR studies, financial support from the IR INFRANALYTICS FR2054 for conducting the research is gratefully acknowledged. Authors also thank the European Cooperation in Science and Technology action (COST MOBIEU, CA15126) for support in Short Term Scientific Missions. Molecular graphics and analyses performed with UCSF Chimera, developed by the Resource for Biocomputing, Visualization, and Informatics at the University of California, San Francisco, with support from NIH P41-GM103311. Authors thank to Dr. Ana Rodríguez-Hortal from the BIO-MS mass spectrometry at the University Pablo de Olavide (Seville) and Dr. Paloma Domínguez-Giménez at the CABIMER microscopy facility (Seville), as well as the microscopy and chromatography services from the Institute of Plant Biochemistry and Photosynthesis (Seville). We also thank Prof. Masami Horikoshi for the kind gift of the plasmid encoding SET/TAF-Iβ ΔC and Dr. Carlos A. Elena-Real for the construction of SET/TAF-Iβ Cys-mutants used in EPR experiments.

AUTHOR CONTRIBUTIONS

M.A.C.-C.: conceptualization, data curation, formal analysis, investigation, methodology, software, writing – original draft, writing – review & editing, visualization. A.V.-C.: formal analysis, writing – review & editing. M.M.: formal analysis. V.B.: formal analysis, writing – review & editing. M.A.R. "De la: conceptualization, funding acquisition, supervision, writing – review & editing. I.D.-M.: conceptualization, funding acquisition, investigation, project administration, supervision, writing – review & editing.

DECLARATION OF INTERESTS

The authors declare no competing interests.

Received: March 11, 2024
Revised: May 16, 2024
Accepted: June 28, 2024
Published: July 2, 2024

REFERENCES

1. Banani, S.F., Lee, H.O., Hyman, A.A., and Rosen, M.K. (2017). Biomolecular condensates: Organizers of cellular biochemistry. Nat. Rev. Mol. Cell Biol. *18*, 285–298. https://doi.org/10.1038/nrm.2017.7.
2. Shin, Y., and Brangwynne, C.P. (2017). Liquid phase condensation in cell physiology and disease. Science *357*, eaaf4382. https://doi.org/10.1126/science.aaf4382.
3. Laflamme, G., and Mekhail, K. (2020). Biomolecular condensates as arbiters of biochemical reactions inside the nucleus. Commun. Biol. *3*, 773. https://doi.org/10.1038/s42003-020-01517-9.
4. O'Flynn, B.G., and Mittag, T. (2021). The role of liquid-liquid phase separation in regulating enzyme activity. Curr. Opin. Cell Biol. *69*, 70–79. https://doi.org/10.1016/j.ceb.2020.12.012.
5. Mehta, S., and Zhang, J. (2022). Liquid–liquid phase separation drives cellular function and dysfunction in cancer. Nat. Rev. Cancer *22*, 239–252. https://doi.org/10.1038/s41568-022-00444-7.
6. Brangwynne, C.P., Eckmann, C.R., Courson, D.S., Rybarska, A., Hoege, C., Gharakhani, J., Jülicher, F., and Hyman, A.A. (2009). Germline P granules are liquid droplets that localize by controlled dissolution/condensation. Science *324*, 1729–1732. https://doi.org/10.1126/science.1172046.
7. Mittag, T., and Parker, R. (2018). Multiple modes of protein-protein interactions promote RNP granule assembly. J. Mol. Biol. *430*, 4636–4649. https://doi.org/10.1016/j.jmb.2018.08.005.
8. Uversky, V.N. (2017). Intrinsically disordered proteins in overcrowded milieu: Membrane-less organelles, phase separation, and intrinsic disorder. Curr. Opin. Struct. Biol. *44*, 18–30. https://doi.org/10.1016/j.sbi.2016.10.015.
9. Yasuhara, T., and Zou, L. (2021). Impacts of chromatin dynamics and compartmentalization on DNA repair. DNA Repair *105*, 103162. https://doi.org/10.1016/j.dnarep.2021.103162.
10. Buchan, J.R., Yoon, J.H., and Parker, R. (2011). Stress-specific composition, assembly and kinetics of stress granules in *Saccharomyces cerevisiae*. J. Cell Sci. *124*, 228–239. https://doi.org/10.1242/jcs.078444.
11. Fefilova, A.S., Fonin, A.V., Vishnyakov, I.E., Kuznetsova, I.M., and Turoverov, K.K. (2022). Stress-induced membraneless organelles in eukaryotes and prokaryotes: bird's-eye view. Int. J. Mol. Sci. *23*, 5010. https://doi.org/10.3390/ijms23095010.
12. Mohanty, P., Kapoor, U., Sundaravadivelu Devarajan, D., Phan, T.M., Rizuan, A., and Mittal, J. (2022). Principles governing the phase separation of multidomain proteins. Biochemistry *61*, 2443–2455. https://doi.org/10.1021/acs.biochem.2c00210.
13. Pak, C.W., Kosno, M., Holehouse, A.S., Padrick, S.B., Mittal, A., Ali, R., Yunus, A.A., Liu, D.R., Pappu, R.V., and Rosen, M.K. (2016). Sequence determinants of intracellular phase separation by complex coacervation of a disordered protein. Mol. Cell *63*, 72–85. https://doi.org/10.1016/j.molcel.2016.05.042.

14. King, M.R., Lin, A.Z., Ruff, K.M., Farag, M., Ouyang, W., Vahey, M.D., Lundberg, E., and Pappu, R.V. (2022). Uncovering molecular grammars of intrinsically disordered regions that organize nucleolar fibrillar centers. Preprint at bioRxiv. https://doi.org/10.1101/2022.11.05.515292.
15. Vernon, R.M., Andrew Chong, P., Tsang, B., Hun Kim, T., Bah, A., Farber, P., Lin, H., and Forman-Kay, J.D. (2018). Pi-pi contacts are an overlooked protein feature relevant to phase separation. Elife *7*, e31486. https://doi.org/10.7554/eLife.31486.
16. Wang, J., Choi, J.M., Holehouse, A.S., Lee, H.O., Zhang, X., Jahnel, M., Maharana, S., Lemaitre, R., Pozniakovsky, A., Drechsel, D., et al. (2018). A Molecular grammar governing the driving forces for phase separation of prion-like RNA binding proteins. Cell *174*, 688–699.e16. https://doi.org/10.1016/j.cell.2018.06.006.
17. Spegg, V., and Altmeyer, M. (2021). Biomolecular condensates at sites of DNA damage: more than just a phase. DNA Repair *106*, 103179. https://doi.org/10.1016/j.dnarep.2021.103179.
18. Sing, C.E., and Perry, S.L. (2020). Recent progress in the science of complex coacervation. Soft Matter *16*, 2885–2914. https://doi.org/10.1039/d0sm00001a.
19. Greig, J.A., Nguyen, T.A., Lee, M., Holehouse, A.S., Posey, A.E., Pappu, R.V., and Jedd, G. (2020). Arginine-enriched mixed-charge domains provide cohesion for nuclear speckle condensation. Mol. Cell *77*, 1237–1250.e4. https://doi.org/10.1016/j.molcel.2020.01.025.
20. Pappu, R.V., Cohen, S.R., Dar, F., Farag, M., and Kar, M. (2023). Phase transitions of associative biomacromolecules. Chem. Rev. *123*, 8945–8987. https://doi.org/10.1021/acs.chemrev.2c00814.
21. Dinic, J., Marciel, A.B., and Tirrell, M.V. (2021). Polyampholyte physics: Liquid–liquid phase separation and biological condensates. Curr. Opin. Colloid Interface Sci. *54*, 101457. https://doi.org/10.1016/j.cocis.2021.101457.
22. Mittag, T., and Pappu, R.V. (2022). A conceptual framework for understanding phase separation and addressing open questions and challenges. Mol. Cell *82*, 2201–2214. https://doi.org/10.1016/j.molcel.2022.05.018.
23. Mohan, A., Oldfield, C.J., Radivojac, P., Vacic, V., Cortese, M.S., Dunker, A.K., and Uversky, V.N. (2006). Analysis of molecular recognition features (MoRFs). J. Mol. Biol. *362*, 1043–1059. https://doi.org/10.1016/j.jmb.2006.07.087.
24. Semenov, A.N., and Rubinstein, M. (1998). Thermoreversible gelation in solutions of associative polymers. 1. Statics. Macromolecules *31*, 1373–1385. https://doi.org/10.1021/ma970616h.
25. Bremer, A., Farag, M., Borcherds, W.M., Peran, I., Martin, E.W., Pappu, R.V., and Mittag, T. (2022). Deciphering how naturally occurring sequence features impact the phase behaviours of disordered prion-like domains. Nat. Chem. *14*, 196–207. https://doi.org/10.1038/s41557-021-00840-w.
26. Choi, J.M., Holehouse, A.S., and Pappu, R.V. (2020). Physical principles underlying the complex biology of intracellular phase transitions. Annu. Rev. Biophys. *49*, 107–133. https://doi.org/10.1146/annurev-biophys-121219-081629.
27. Cohan, M.C., Shinn, M.K., Lalmansingh, J.M., and Pappu, R.V. (2022). Uncovering non-random binary patterns within sequences of intrinsically disordered proteins. J. Mol. Biol. *434*, 167373. https://doi.org/10.1016/j.jmb.2021.167373.
28. Zarin, T., Strome, B., Peng, G., Pritišanac, I., Forman-Kay, J.D., and Moses, A.M. (2021). Identifying molecular features that are associated with biological function of intrinsically disordered protein regions. Elife *10*, e60220. https://doi.org/10.7554/eLife.60220.
29. Ruff, K.M., Choi, Y.H., Cox, D., Ormsby, A.R., Myung, Y., Ascher, D.B., Radford, S.E., Pappu, R.V., and Hatters, D.M. (2022). Sequence grammar underlying the unfolding and phase separation of globular proteins. Mol. Cell *82*, 3193–3208.e8. https://doi.org/10.2139/ssrn.3929009.
30. Zhou, H.X., Nguemaha, V., Mazarakos, K., and Qin, S. (2018). Why do disordered and structured proteins behave differently in phase separation? Trends Biochem. Sci. *43*, 499–516. https://doi.org/10.1016/j.tibs.2018.03.007.
31. Banjade, S., Wu, Q., Mittal, A., Peeples, W.B., Pappu, R.V., and Rosen, M.K. (2015). Conserved interdomain linker promotes phase separation of the multivalent adaptor protein Nck. Proc. Natl. Acad. Sci. USA *112*, e6426–e6435. https://doi.org/10.1073/pnas.1508778112.
32. Martínez-Fábregas, J., Díaz-Moreno, I., González-Arzola, K., Janochas, S., Navarro, J.A., Hervás, M., Bernhardt, R., Velázquez-Campoy, A., Díaz-Quintana, A., and De la Rosa, M.A. (2014). Structural and functional analysis of novel human cytochrome *c* targets in apoptosis. Mol. Cell. Proteomics *13*, 1439–1456. https://doi.org/10.1074/mcp.M113.034322.
33. Martínez-Fábregas, J., Díaz-Moreno, I., González-Arzola, K., Díaz-Quintana, A., and De la Rosa, M.A. (2014). A common signalosome for programmed cell death in humans and plants. Cell Death Dis. *5*, e1314. https://doi.org/10.1038/cddis.2014.280.
34. González-Arzola, K., Díaz-Quintana, A., Bernardo-García, N., Martínez-Fábregas, J., Rivero-Rodríguez, F., Casado-Combreras, M.Á., Elena-Real, C.A., Velázquez-Cruz, A., Gil-Caballero, S., Velázquez-Campoy, A., et al. (2022). Nucleus-translocated mitochondrial cytochrome *c* liberates nucleophosmin-sequestered ARF tumor suppressor by changing nucleolar liquid-liquid phase separation. Nat. Struct. Mol. Biol. *29*, 1024–1036. https://doi.org/10.1038/s41594-022-00842-3.
35. Martelli, F., Hamilton, T., Silver, D.P., Sharpless, N.E., Bardeesy, N., Rokas, M., DePinho, R.A., Livingston, D.M., and Grossman, S.R. (2001). p19ARF targets certain E2F species for degradation. Proc. Natl. Acad. Sci. USA *98*, 4455–4460. https://doi.org/10.1073/pnas.081061398.
36. Okuwaki, M., and Nagata, K. (1998). Template activating factor-I remodels the chromatin structure and stimulates transcription from the chromatin template. J. Biol. Chem. *273*, 34511–34518. https://doi.org/10.1074/jbc.273.51.34511.
37. Estanyol, J.M., Jaumot, M., Casanovas, O., Rodríguez-Vilarrupla, A., Agell, N., and Bachs, O. (1999). The protein SET regulates the inhibitory effect of p21(Cip1) on cyclin E-cyclin-dependent kinase 2 activity. J. Biol. Chem. *274*, 33161–33165. https://doi.org/10.1074/jbc.274.46.33161.
38. Fan, Z., Beresford, P.J., Oh, D.Y., Zhang, D., and Lieberman, J. (2003). Tumor suppressor NM23-H1 is a Granzyme A-activated DNase during CTL-mediated apoptosis, and the nucleosome assembly protein SET is its inhibitor. Cell *112*, 659–672. https://doi.org/10.1016/s0092-8674(03)00150-8.
39. Muto, S., Senda, M., Akai, Y., Sato, L., Suzuki, T., Nagai, R., Senda, T., and Horikoshi, M. (2007). Relationship between the structure of SET/TAF-Ibeta/INHAT and its histone chaperone activity. Proc. Natl. Acad. Sci. USA *104*, 4285–4290. https://doi.org/10.1073/pnas.0603762104.
40. Kato, K., Okuwaki, M., and Nagata, K. (2011). Role of Template Activating Factor-I as a chaperone in linker histone dynamics. J. Cell Sci. *124*, 3254–3265. https://doi.org/10.1242/jcs.083139.
41. Kalousi, A., Hoffbeck, A.S., Selemenakis, P.N., Pinder, J., Savage, K.I., Khanna, K.K., Brino, L., Dellaire, G., Gorgoulis, V.G., and Soutoglou, E. (2015). The nuclear oncogene SET controls DNA repair by KAP1 and HP1 retention to chromatin. Cell Rep. *11*, 149–163. https://doi.org/10.1016/j.celrep.2015.03.005.
42. Mandemaker, I.K., Zhou, D., Bruens, S.T., Dekkers, D.H., Verschure, P.J., Edupuganti, R.R., Meshorer, E., Demmer, J.A., and Marteijn, J.A. (2020). Histone H1 eviction by the histone chaperone SET reduces cell survival following DNA damage. J. Cell Sci. *133*, jcs235473. https://doi.org/10.1242/jcs.235473.
43. González-Arzola, K., Díaz-Moreno, I., Cano-González, A., Díaz-Quintana, A., Velázquez-Campoy, A., Moreno-Beltrán, B., López-Rivas, A., and De la Rosa, M.A. (2015). Structural basis for inhibition of the histone chaperone activity of SET/TAF-Iβ by cytochrome *c*. Proc. Natl. Acad. Sci. USA *112*, 9908–9913. https://doi.org/10.1073/pnas.1508040112.
44. Casado-Combreras, M.Á., Rivero-Rodríguez, F., Elena-Real, C.A., Molodenskiy, D., Díaz-Quintana, A., Martinho, M., Gerbaud, G., González-Arzola, K., Velázquez-Campoy, A., Svergun, D., et al. (2022). PP2A is activated by cytochrome *c* upon formation of a diffuse encounter complex with SET/TAF-Iβ. Comput. Struct. Biotechnol. J. *20*, 3695–3707. https://doi.org/10.1016/j.csbj.2022.07.009.
45. Li, M., Makkinje, A., and Damuni, Z. (1996). The myeloid leukemia-associated protein SET is a potent inhibitor of protein phosphatase 2A. J. Biol. Chem. *271*, 11059–11062. https://doi.org/10.1074/jbc.271.19.11059.
46. Altmeyer, M., Neelsen, K.J., Teloni, F., Pozdnyakova, I., Pellegrino, S., Grøfte, M., Rask, M.B.D., Streicher, W., Jungmichel, S., Nielsen, M.L., and Lukas, J. (2015). Liquid demixing of intrinsically disordered proteins is seeded by poly(ADP-ribose). Nat. Commun. *6*, 8088. https://doi.org/10.1038/ncomms9088.
47. Kilic, S., Lezaja, A., Gatti, M., Bianco, E., Michelena, J., Imhof, R., and Altmeyer, M. (2019). Phase separation of 53BP1 determines liquid-like behavior of DNA repair compartments. EMBO J. *38*, e101379. https://doi.org/10.15252/embj.2018101379.
48. Larson, A.G., Elnatan, D., Keenen, M.M., Trnka, M.J., Johnston, J.B., Burlingame,

A.L., Agard, D.A., Redding, S., and Narlikar, G.J. (2017). Liquid droplet formation by HP1α suggests a role for phase separation in heterochromatin. Nature *547*, 236–240. https://doi.org/10.1038/nature22822.

49. Sanulli, S., Trnka, M.J., Dharmarajan, V., Tibble, R.W., Pascal, B.D., Burlingame, A.L., Griffin, P.R., Gross, J.D., and Narlikar, G.J. (2019). HP1 reshapes nucleosome core to promote phase separation of heterochromatin. Nature *575*, 390–394. https://doi.org/10.1038/s41586-019-1669-2.
50. Karetsou, Z., Emmanouilidou, A., Sanidas, I., Liokatis, S., Nikolakaki, E., Politou, A.S., and Papamarcaki, T. (2009). Identification of distinct SET/TAF-Ibeta domains required for core histone binding and quantitative characterisation of the interaction. BMC Biochem. *10*, 10. https://doi.org/10.1186/1471-2091-10-10.
51. Box, J.K., Paquet, N., Adams, M.N., Boucher, D., Bolderson, E., O'Byrne, K.J., and Richard, D.J. (2016). Nucleophosmin: from structure and function to disease development. BMC Mol. Biol. *17*, 19. https://doi.org/10.1186/s12867-016-0073-9.
52. Banani, S.F., Rice, A.M., Peeples, W.B., Lin, Y., Jain, S., Parker, R., and Rosen, M.K. (2016). Compositional control of phase-separated cellular bodies. Cell *166*, 651–663. https://doi.org/10.1016/j.cell.2016.06.010.
53. Feric, M., Vaidya, N., Harmon, T.S., Mitrea, D.M., Zhu, L., Richardson, T.M., Kriwacki, R.W., Pappu, R.V., and Brangwynne, C.P. (2016). Coexisting liquid phases underlie nucleolar subcompartments. Cell *165*, 1686–1697. https://doi.org/10.1016/j.cell.2016.04.047.
54. Mitrea, D.M., Cika, J.A., Guy, C.S., Ban, D., Banerjee, P.R., Stanley, C.B., Nourse, A., Deniz, A.A., and Kriwacki, R.W. (2016). Nucleophosmin integrates within the nucleolus via multi-modal interactions with proteins displaying R-rich linear motifs and rRNA. Elife *5*, e13571. https://doi.org/10.7554/elife.13571.
55. Mitrea, D.M., Grace, C.R., Buljan, M., Yun, M.K., Pytel, N.J., Satumba, J., Nourse, A., Park, C.G., Babu, M.M., White, S.W., and Kriwacki, R.W. (2014). Structural polymorphism in the N-terminal oligomerization domain of NPM1. Proc. Natl. Acad. Sci. USA *111*, 4466–4471. https://doi.org/10.1073/pnas.1321007111.
56. Mitrea, D.M., Cika, J.A., Stanley, C.B., Nourse, A., Onuchic, P.L., Banerjee, P.R., Phillips, A.H., Park, C.G., Deniz, A.A., and Kriwacki, R.W. (2018). Self-interaction of NPM1 modulates multiple mechanisms of liquid-liquid phase separation. Nat. Commun. *9*, 842. https://doi.org/10.1038/s41467-018-03255-3.
57. Mitrea, D.M., and Kriwacki, R.W. (2018). On the relationship status for Arf and NPM1 - it's complicated. FEBS J. *285*, 828–831. https://doi.org/10.1111/febs.14407.
58. Webb, B., and Sali, A. (2017). Protein structure modeling with MODELLER. Methods Mol. Biol. *1654*, 39–54. https://doi.org/10.1007/978-1-4939-7231-9_4.
59. Gallo, A., Lo Sterzo, C., Mori, M., Di Matteo, A., Bertini, I., Banci, L., Brunori, M., and Federici, L. (2012). Structure of nucleophosmin DNA-binding domain and analysis of its complex with a G-quadruplex sequence from the c-MYC promoter. J. Biol. Chem. *287*, 26539–26548. https://doi.org/10.1074/jbc.m112.371013.
60. Capaldi, R.A., Darley-Usmar, V., Fuller, S., and Millett, F. (1982). Structural and functional features of the interaction of cytochrome *c* with complex III and cytochrome *c* oxidase. FEBS Lett. *138*, 1–7. https://doi.org/10.1016/0014-5793(82)80382-7.
61. Navarro, J.A., Hervás, M., Genzor, C.G., Cheddar, G., Fillat, M.F., De la Rosa, M.A., Gómez-Moreno, C., Cheng, H., Xia, B., Chae, Y.K., et al. (1995). Site-specific mutagenesis demonstrates that the structural requirements for efficient electron transfer in *Anabaena* ferredoxin and flavodoxin are highly dependent on the reaction partner: kinetic studies with photosystem I, ferredoxin:NADP+ reductase, and cytochrome *c*. Arch. Biochem. Biophys. *321*, 229–238. https://doi.org/10.1006/abbi.1995.1390.
62. Kurki, S., Peltonen, K., Latonen, L., Kiviharju, T.M., Ojala, P.M., Meek, D., and Laiho, M. (2004). Nucleolar protein NPM interacts with HDM2 and protects tumor suppressor protein p53 from HDM2-mediated degradation. Cancer Cell *5*, 465–475. https://doi.org/10.1016/s1535-6108(04)00110-2.
63. Jones, S., Holm, T., Mäger, I., Langel, Ü., and Howl, J. (2010). Characterization of bioactive cell penetrating peptides from human cytochrome *c*: Protein mimicry and the development of a novel apoptogenic agent. Chem. Biol. *17*, 735–744. https://doi.org/10.1016/j.chembiol.2010.05.018.
64. Imai, M., Saio, T., Kumeta, H., Uchida, T., Inagaki, F., and Ishimori, K. (2016). Investigation of the redox-dependent modulation of structure and dynamics in human cytochrome *c*. Biochem. Biophys. Res. Commun. *469*, 978–984. https://doi.org/10.1016/j.bbrc.2015.12.079.
65. Levone, B.R., Lenzken, S.C., Antonaci, M., Maiser, A., Rapp, A., Conte, F., Reber, S., Mechtersheimer, J., Ronchi, A.E., Mühlemann, O., et al. (2021). FUS-dependent liquid-liquid phase separation is important for DNA repair initiation. J. Cell Biol. *220*, e202008030. https://doi.org/10.1083/jcb.202008030.
66. Gracia, P., Polanco, D., Tarancón-Díez, J., Serra, I., Bracci, M., Oroz, J., Laurents, D.V., García, I., and Cremades, N. (2022). Molecular mechanism for the synchronized electrostatic coacervation and co-aggregation of alpha-synuclein and tau. Nat. Commun. *13*, 4586. https://doi.org/10.1038/s41467-022-32350-9.
67. Molliex, A., Temirov, J., Lee, J., Coughlin, M., Kanagaraj, A.P., Kim, H.J., Mittag, T., and Taylor, J.P. (2015). Phase separation by low complexity domains promotes stress granule assembly and drives pathological fibrillization. Cell *163*, 123–133. https://doi.org/10.1016/j.cell.2015.09.015.
68. Fossat, M.J., Zeng, X., and Pappu, R.V. (2021). Uncovering differences in hydration free energies and structures for model compound mimics of charged side chains of amino acids. J. Phys. Chem. B *125*, 4148–4161. https://doi.org/10.1021/acs.jpcb.1c01073.
69. Zeng, X., Ruff, K.M., and Pappu, R.V. (2022). Competing interactions give rise to two-state behavior and switch-like transitions in charge-rich intrinsically disordered proteins. Proc. Natl. Acad. Sci. USA *119*, e2200559119. https://doi.org/10.1073/pnas.2200559119.
70. Ukmar-Godec, T., Hutten, S., Grieshop, M.P., Rezaei-Ghaleh, N., Cima-Omori, M.S., Biernat, J., Mandelkow, E., Söding, J., Dormann, D., and Zweckstetter, M. (2019). Lysine/RNA-interactions drive and regulate biomolecular condensation. Nat. Commun. *10*, 2909. https://doi.org/10.1038/s41467-019-10792-y.
71. Cooper, A. (2005). Heat capacity effects in protein folding and ligand binding: a re-evaluation of the role of water in biomolecular thermodynamics. Biophys. Chem. *115*, 89–97. https://doi.org/10.1016/j.bpc.2004.12.011.
72. Pylaeva, S., Brehm, M., and Sebastiani, D. (2018). Salt bridge in aqueous solution: strong structural motifs but weak enthalpic effect. Sci. Rep. *8*, 13626. https://doi.org/10.1038/s41598-018-31935-z.
73. Cho, B., Choi, J., Kim, R., Yun, J.N., Choi, Y., Lee, H.H., and Koh, J. (2021). Thermodynamic models for assembly of intrinsically disordered protein hubs with multiple interaction partners. J. Am. Chem. Soc. *143*, 12509–12523. https://doi.org/10.1021/jacs.1c00811.
74. Mukherjee, S., and Schäfer, L.V. (2023). Thermodynamic forces from protein and water govern condensate formation of an intrinsically disordered protein domain. Nat. Commun. *14*, 5892. https://doi.org/10.1038/s41467-023-41586-y.
75. Mollica, L., Bessa, L.M., Hanoulle, X., Jensen, M.R., Blackledge, M., and Schneider, R. (2016). Binding mechanisms of intrinsically disordered proteins: Theory, simulation, and experiment. Front. Mol. Biosci. *3*, 52. https://doi.org/10.3389/fmolb.2016.00052.
76. Falahati, H., and Haji-Akbari, A. (2019). Thermodynamically driven assemblies and liquid-liquid phase separations in biology. Soft Matter *15*, 1135–1154. https://doi.org/10.1039/c8sm02285b.
77. Guseva, S., Schnapka, V., Adamski, W., Maurin, D., Ruigrok, R.W.H., Salvi, N., and Blackledge, M. (2023). Liquid–liquid phase separation modifies the dynamic properties of intrinsically disordered proteins. J. Am. Chem. Soc. *145*, 10548–10563. https://doi.org/10.1021/jacs.2c13647.
78. Banci, L., Bertini, I., De la Rosa, M.A., Koulougliotis, D., Navarro, J.A., and Walter, O. (1998). Solution structure of oxidized cytochrome c_6 from the green alga *Monoraphidium braunii*. Biochemistry *37*, 4831–4843. https://doi.org/10.1021/bi972765y.
79. Blauer, G., Sreerama, N., and Woody, R.W. (1993). Optical activity of hemoproteins in the Soret region. Circular dichroism of the heme undecapeptide of cytochrome *c* in aqueous solution. Biochemistry *32*, 6674–6679. https://doi.org/10.1021/bi00077a021.
80. Navarro, J.A., Hervás, M., De la Cerda, B., and De la Rosa, M.A. (1995). Purification and physicochemical properties of the low-potential cytochrome c_{549} from the cyanobacterium *Synechocystis* sp. PCC 6803. Arch. Biochem. Biophys. *318*, 46–52. https://doi.org/10.1006/abbi.1995.1202.
81. Díaz, A., Navarro, F., Hervás, M., Navarro, J.A., Chávez, S., Florencio, F.J., and De la Rosa, M.A. (1994). Cloning and correct expression in *E. coli* of the *petJ* gene encoding cytochrome c_6 from *Synechocystis* 6803. FEBS Lett. *347*, 173–177. https://doi.org/10.1016/0014-5793(94)00529-x.

82. Fitch, C.A., Platzer, G., Okon, M., Garcia-Moreno, B.E., and McIntosh, L.P. (2015). Arginine: its pKa value revisited. Protein Sci. *24*, 752–761. https://doi.org/10.1002/pro.2647.
83. Gobbi, A., and Frenking, G. (1993). Y-conjugated compounds: the equilibrium geometries and electronic structures of guanidine, guanidinium cation, urea, and 1,1-diaminoethylene. J. Am. Chem. Soc. *115*, 2362–2372. https://doi.org/10.1021/ja00059a035.
84. Alberti, S., Saha, S., Woodruff, J.B., Franzmann, T.M., Wang, J., and Hyman, A.A. (2018). A user's guide for phase separation assays with purified proteins. J. Mol. Biol. *430*, 4806–4820. https://doi.org/10.1016/j.jmb.2018.06.038.
85. Ray, S., Singh, N., Patel, K., Krishnamoorthy, G., and Maji, S.K. (2023). FRAP and FRET investigation of α-synuclein fibrillization via liquid-liquid phase separation *in vitro* and in HeLa cells. Methods Mol. Biol. *2551*, 395–423. https://doi.org/10.1007/978-1-0716-2597-2_26.
86. Shiina, N. (2019). Liquid- and solid-like RNA granules form through specific scaffold proteins and combine into biphasic granules. J. Biol. Chem. *294*, 3532–3548. https://doi.org/10.1074/jbc.RA118.005423.
87. Patel, A., Lee, H.O., Jawerth, L., Drechsel, D., Hyman, A.A., Alberti, S., Maharana, S., Jahnel, M., Hein, M.Y., Stoynov, S., et al. (2015). A liquid-to-solid phase transition of the ALS protein FUS accelerated by disease mutation. Cell *162*, 1066–1077. https://doi.org/10.1016/j.cell.2015.07.047.
88. Xu, B., He, G., Weiner, B.G., Ronceray, P., Meir, Y., Jonikas, M.C., and Wingreen, N.S. (2020). Rigidity enhances a magic-number effect in polymer phase separation. Nat. Commun. *11*, 1561. https://doi.org/10.1038/s41467-020-15395-6.
89. Ahn, J.I., Park, J.-E., Meng, L., Zhang, L., Kim, T.-S., Kruhlak, M.J., Kim, B.Y., and Lee, K.S. (2020). Phase separation of the Cep63·Cep152 complex underlies the formation of dynamic supramolecular self-assemblies at human centrosomes. Cell Cycle *19*, 3437–3457. https://doi.org/10.1080/15384101.2020.1843777.
90. Sabari, B.R., Dall'Agnese, A., and Young, R.A. (2020). Biomolecular condensates in the nucleus. Trends Biochem. Sci. *45*, 961–977. https://doi.org/10.1016/j.tibs.2020.06.007.
91. Singatulina, A.S., Hamon, L., Sukhanova, M.V., Desforges, B., Joshi, V., Bouhss, A., Lavrik, O.I., and Paste, D. (2019). PARP-1 activation directs FUS to DNA damage sites to form PARG-reversible compartments enriched in damaged DNA. Cell Rep. *27*, 1809–1821.e5. https://doi.org/10.1016/j.celrep.2019.04.031.
92. Zgheib, O., Pataky, K., Brugger, J., and Halazonetis, T.D. (2009). An oligomerized 53BP1 tudor domain suffices for recognition of DNA double-strand breaks. Mol. Cell Biol. *29*, 1050–1058. https://doi.org/10.1128/MCB.01011-08.
93. Mittag, T., Marsh, J., Grishaev, A., Orlicky, S., Lin, H., Sicheri, F., Tyers, M., and Forman-Kay, J.D. (2010). Structure/function implications in a dynamic complex of the intrinsically disordered Sic1 with the Cdc4 subunit of an SCF ubiquitin ligase. Structure *18*, 494–506. https://doi.org/10.1016/j.str.2010.01.020.
94. Rivero-Rodríguez, F., Díaz-Quintana, A., Velázquez-Cruz, A., González-Arzola, K., Gavilan, M.P., Velázquez-Campoy, A., Ríos, R.M., De la Rosa, M.A., and Díaz-Moreno, I. (2021). Inhibition of the PP2A activity by the histone chaperone ANP32B is long-range allosterically regulated by respiratory cytochrome *c*. Redox Biol. *43*, 101967. https://doi.org/10.1016/j.redox.2021.101967.
95. Mahadevi, A.S., and Sastry, G.N. (2016). Cooperativity in noncovalent interactions. Chem. Rev. *116*, 2775–2825. https://doi.org/10.1021/cr500344e.
96. Choi, J., Hyman, A.A., and Pappu, R.V. (2020). Generalized models for bond percolation transitions of associative polymers. Phys. Rev. E *102*, 042403. https://doi.org/10.1103/PhysRevE.102.042403.
97. Murray, D.T., Kato, M., Lin, Y., Thurber, K.R., Hung, I., McKnight, S.L., and Tycko, R. (2017). Structure of FUS protein fibrils and its relevance to self-assembly and phase separation of low-complexity domains. Cell *171*, 615–627.e16. https://doi.org/10.1016/j.cell.2017.08.048.
98. Carlson, C.R., Asfaha, J.B., Ghent, C.M., Howard, C.J., Hartooni, N., Safari, M., Frankel, A.D., and Morgan, D.O. (2020). Phosphoregulation of phase separation by the SARS-CoV-2 N protein suggests a biophysical basis for its dual functions. Mol. Cell *80*, 1092–1103.e4. https://doi.org/10.1016/j.molcel.2020.11.025.
99. Buzón, P., Velázquez-Cruz, A., Corrales-Guerrero, L., Díaz-Quintana, A., Díaz-Moreno, I., and Roos, W.H. (2023). The histone chaperones SET/TAF-1β and NPM1 exhibit conserved functionality in nucleosome remodeling and histone eviction in a cytochrome *c*-dependent manner. Adv. Sci. *10*, e2301859. https://doi.org/10.1002/advs.202301859.
100. Díaz-Moreno, I., Velázquez-Cruz, A., Curran-French, S., Díaz-Quintana, A., and De la Rosa, M.A. (2018). Nuclear cytochrome *c* – a mitochondrial visitor regulating damaged chromatin dynamics. FEBS Lett. *592*, 172–178. https://doi.org/10.1002/1873-3468.12959.
101. Ramazi, S., and Zahiri, J. (2021). Post-translational modifications in proteins: resources, tools and prediction methods. Database *2021*, baab012. https://doi.org/10.1093/database/baab012.
102. Kim, S.C., Sprung, R., Chen, Y., Xu, Y., Ball, H., Pei, J., Cheng, T., Kho, Y., Xiao, H., Xiao, L., et al. (2006). Substrate and functional diversity of lysine acetylation revealed by a proteomics survey. Mol. Cell *23*, 607–618. https://doi.org/10.1016/j.molcel.2006.06.026.
103. Bazylianska, V., Kalpage, H.A., Wan, J., Vaishnav, A., Mahapatra, G., Turner, A.A., Chowdhury, D.D., Kim, K., Morse, P.T., Lee, I., et al. (2021). Lysine 53 acetylation of cytochrome *c* in prostate cancer: Warburg metabolism and evasion of apoptosis. Cells *10*, 802. https://doi.org/10.3390/cells10040802.
104. Morse, P.T., Pérez-Mejías, G., Wan, J., Turner, A.A., Márquez, I., Kalpage, H.A., Vaishnav, A., Zurek, M.P., Huettemann, P.P., Kim, K., et al. (2023). Cytochrome *c* lysine acetylation regulates cellular respiration and cell death in ischemic skeletal muscle. Nat. Commun. *14*, 4166. https://doi.org/10.1038/s41467-023-39820-8.
105. Prakash, H., and Mazumdar, S. (2009). Succinylation of cytochrome *c* investigated by electrospray ionization mass spectrometry: reactive lysine residues. Int. J. Mass Spectrom. *281*, 55–62. https://doi.org/10.1016/j.ijms.2008.12.013.
106. Boeynaems, S., Alberti, S., Fawzi, N.L., Mittag, T., Polymenidou, M., Rousseau, F., Schymkowitz, J., Shorter, J., Wolozin, B., Van Den Bosch, L., et al. (2018). Protein phase separation: a new phase in cell biology. Trends Cell Biol. *28*, 420–435. https://doi.org/10.1016/j.tcb.2018.02.004.
107. Olteanu, A., Patel, C.N., Dedmon, M.M., Kennedy, S., Linhoff, M.W., Minder, C.M., Potts, P.R., Deshmukh, M., and Pielak, G.J. (2003). Stability and apoptotic activity of recombinant human cytochrome *c*. Biochem. Biophys. Res. Commun. *312*, 733–740. https://doi.org/10.1016/j.bbrc.2003.10.182.
108. Tian, C., Kasavajhala, K., Belfon, K.A.A., Raguette, L., Huang, H., Migues, A.N., Bickel, J., Wang, Y., Pincay, J., Wu, Q., and Simmerling, C. (2020). ff19SB: Amino-acid-specific protein backbone parameters trained against quantum mechanics energy surfaces in solution. J. Chem. Theory Comput. *16*, 528–552. https://doi.org/10.1021/acs.jctc.9b00591.
109. Autenrieth, F., Tajkhorshid, E., Baudry, J., and Luthey-Schulten, Z. (2004). Classical force field parameters for the heme prosthetic group of cytochrome *c*. J. Comput. Chem. *25*, 1613–1622. https://doi.org/10.1002/jcc.20079.
110. Pecina, P., Borisenko, G.G., Belikova, N.A., Tyurina, Y.Y., Pecinova, A., Lee, I., Samhan-Arias, A.K., Przyklenk, K., Kagan, V.E., and Hüttemann, M. (2010). Phosphomimetic substitution of cytochrome *c* tyrosine 48 decreases respiration and binding to cardiolipin and abolishes ability to trigger downstream caspase activation. Biochemistry *49*, 6705–6714. https://doi.org/10.1021/bi100486s.
111. Eastman, P., Swails, J., Chodera, J.D., McGibbon, R.T., Zhao, Y., Beauchamp, K.A., Wang, L.-P., Simmonett, A.C., Harrigan, M.P., Stern, C.D., et al. (2017). OpenMM 7: Rapid development of high performance algorithms for molecular dynamics. PLoS Comput. Biol. *13*, e1005659. https://doi.org/10.1371/journal.pcbi.1005659.
112. Case, D., Betz, R., Cerutti, D., Cheatham III, T., Darden, T., Duke, R., Giese, T., Gohlke, H., Goetz, A., Homeyer, N., et al. (2016). AMBER (University of California).
113. Pettersen, E.F., Goddard, T.D., Huang, C.C., Couch, G.S., Greenblatt, D.M., Meng, E.C., and Ferrin, T.E. (2004). UCSF Chimera - a visualization system for exploratory research and analysis. J. Comput. Chem. *25*, 1605–1612. https://doi.org/10.1002/jcc.20084.
114. Jurrus, E., Engel, D., Star, K., Monson, K., Brandi, J., Felberg, L.E., Brookes, D.H., Wilson, L., Chen, J., Liles, K., et al. (2018). Improvements to the APBS biomolecular solvation software suite. Protein Sci. *27*, 112–128. https://doi.org/10.1002/pro.3280.
115. Dolinsky, T.J., Nielsen, J.E., McCammon, J.A., and Baker, N.A. (2004). PDB2PQR: an automated pipeline for the setup of Poisson-Boltzmann electrostatics calculations. Nucleic Acids Res. *32*, W665–W667. https://doi.org/10.1093/nar/gkh381.
116. Schindelin, J., Arganda-Carreras, I., Frise, E., Kaynig, V., Longair, M., Pietzsch, T., Preibisch, S., Rueden, C., Saalfeld, S., Schmid, B., et al. (2012). Fiji: An open-source platform for biological-image analysis. Nat.

Methods *9*, 676–682. https://doi.org/10.1038/nmeth.2019.

117. Moreno-Beltrán, B., Díaz-Moreno, I., González-Arzola, K., Guerra-Castellano, A., Velázquez-Campoy, A., De La Rosa, M.A., and Díaz-Quintana, A. (2015). Respiratory complexes III and IV can each bind two molecules of cytochrome *c* at low ionic strength. FEBS Lett. *589*, 476–483. https://doi.org/10.1016/j.febslet.2015.01.004.
118. Bradford, M.M. (1976). A rapid and sensitive method for the quantitation of microgram quantities of protein utilizing the principle of protein-dye binding. Anal. Biochem. *72*, 248–254. https://doi.org/10.1006/abio.1976.9999.
119. Roumestand, C., and Canet, D. (2000). Extending the excitation sculpting concept for selective excitation. J. Magn. Reson. *147*, 331–339. https://doi.org/10.1006/jmre.2000.2206.
120. Izadi, S., Anandakrishnan, R., and Onufriev, A.V. (2014). Building water models: a different approach. J. Phys. Chem. Lett. *5*, 3863–3871. https://doi.org/10.1021/jz501780a.
121. Andersen, H.C. (1980). Molecular dynamics simulations at constant pressure and/or temperature. J. Chem. Phys. *72*, 2384–2393. https://doi.org/10.1063/1.439486.
122. Roe, D.R., and Cheatham, T.E. (2013). PTRAJ and CPPTRAJ: software for processing and analysis of molecular dynamics trajectory data. J. Chem. Theory Comput. *9*, 3084–3095. https://doi.org/10.1021/ct400341p.

STAR★METHODS

KEY RESOURCES TABLE

REAGENT or RESOURCE	SOURCE	IDENTIFIER
Bacterial and virus strains		
Escherichia coli DH5α	Homemade	N/A
Escherichia coli BL21(DE3	Homemade	N/A
Escherichia coli C43(DE3)	Homemade	N/A
Chemicals, peptides, and recombinant proteins		
SET/TAF-Iβ	Martínez-Fábregas et al.[32]	https://doi.org/10.1074/mcp.M113.034322.
SET/TAF-Iβ Q69C mutant	This manuscript	N/A
SET/TAF-Iβ D226C mutant	This manuscript	N/A
SET/TAF-Iβ E243C mutant	This manuscript	N/A
SET/TAF-Iβ D260C mutant	This manuscript	N/A
SET/TAF-Iβ D277C mutant	This manuscript	N/A
SET/TAF-Iβ ΔC	Muto et al.[39]	https://doi.org/10.1073/pnas.0603762104
SET/TAF-Iβ ΔC Q69C mutant	Casado-Combreras et al.[44]	https://doi.org/10.1016/j.csbj.2022.07.009
NPM1	González-Arzola et al.[34]	https://doi.org/10.1038/s41594-022-00842-3
Cytochrome *c*	Olteanu et al.[107]	https://doi.org/10.1016/j.bbrc.2003.10.182
Cytochrome *c* K5A/K7A/K8A mutant	This manuscript	N/A
Cytochrome *c* K5R/K7R/K8R mutant	This manuscript	N/A
Cytochrome *c* K86A/K87A/K88A mutant	This manuscript	N/A
Cytochrome *c* K86R/K87R/K88R mutant	This manuscript	N/A
MTSL ([1-oxyl-2,2,5,5-tetramethyl-δ3-pyrroline-3-methyl] methanethiosulfonate)	*Toronto Research Chemicals Inc.*	Cat. n.: TRC-O875000
Oregon Green™ 488 maleimide probe (*Molecular Probes*)	*Invitrogen/ThermoFisher*	Cat. n.: O6034
Texas Red™-X succinimidyl ester probe (*Molecular Probes*)	*Invitrogen/ThermoFisher*	Cat. n.: T20175
Ficoll^{R} PM70	*Cytiva*	Cat. n.: 17-0310-50
OmniPur® DTT (Dithiothreitol)	*CalBioChem*	Cat. n.: 3870-25GM
NcoI (restriction enzyme)	*New England Biolabs*	Cat. n.: R0193S
BamHI-HF (restriction enzyme)	*New England Biolabs*	Cat. n.: R3136S
DpnI (restriction enzyme)	*Roche/Merck*	Cat. n.: 10642988001/DPNI-RO
T4 DNA ligase	*New England Biolabs*	Cat. n.: M0202S
Dimethyl sulfoxide (DMSO)	*PanReac AppliChem*	Cat. n.: A3672.0100
Lysozyme	*Thermo Scientific*	Cat. n.: 89833
DNase I	*Roche*	Cat. n.: 10104159001
Phenylmethylsulphonyl fluoride (PMSF)	*Sigma Aldrich*	Cat. n.: 93482-50ML-F
cOmplete™ Mini, EDTA-free	*Roche*	Cat. n.: 04693132001
BioRad Protein assay dye reagent concentrate	*BioRad*	Cat. n.: #5000006
Critical commercial assays		
In-Fusion™ Snap Assembly EcoDry system	*Takara Bio*	Cat. n.: 638954
KOD Hot Start DNA Polymerase	*Sigma Aldrich*	Cat. n.: 71086-5
NucleoSpin Gel and PCR Clean-Up Kit	*Macherey-Nagel*	Cat. n.: 740609.50S
GenElute™ plasmid miniprep kit	*Sigma Aldrich*	Cat. n.: PLN70-1KT

(*Continued on next page*)

Continued

REAGENT or RESOURCE	SOURCE	IDENTIFIER
Deposited data		
SET/TAF-Iβ ΔC structure (XRD)	Muto et al.[39]	PDB (entry 2E50)
$NPM1_{1-130}$ structure (oligomerization domain, XRD)	Mitrea et al.[55]	PDB (entry 4N8M)
$NPM1_{226-294}$ structure (DNA binding domain, NMR)	Gallo et al.[59]	PDB (entry 2LLH)
Reduced human cytochrome *c* structure (NMR)	Imai et al.[64]	PDB (entry 2N9I)
Human cytochrome *c* structure (XRD)	Rajagopal et al. (2013) [S6]	PDB (entry 3ZCF)
HDM2 RING finger domain structure (NMR)	Kostic et al. (2006) [S7]	PDB (entry 2HDP)
[^{1}H-^{15}N] HSQC-NMR titrations of reduced cytochrome *c* with SET/TAF-Iβ	González-Arzola et al.[43]	https://doi.org/10.1073/pnas.1508040112
[^{1}H-^{15}N] HSQC-NMR titrations of reduced cytochrome *c* with NPM1	González-Arzola et al.[34]	https://doi.org/10.1038/s41594-022-00842-3
ff19SB force-field libraries	Tian et al.[108]	https://ambermd.org/AmberModels.php
Force-field parameters for the heme group	Autenrieth et al.[109]	https://doi.org/10.1002/jcc.20079
Oligonucleotides		
Primers used for DNA amplification, molecular cloning and mutagenesis	This manuscript	See supplemental information (Table S5)
Recombinant DNA		
K5R/K7R/K8R Cc-encoding gBlock: 5′ - ATGGGCGACGTGGAAAGGGGCAGGAGGATC TTCATCATGAAATGCTCGCAGTGCCACACGGTGG AAAAAGGCGGCAAACACAAAACCGGTCCCAACC TGCACGGCCTGTTCGGCCGCAAAACGGGCCAGG CGCCGGGCTACAGCTACACGGCGGCGAACAAAA ACAAAGGCATCATCTGGGGCGAAGACACGCTGAT GGAATACCTCGAGAACCCGAAAAAATACATCCCG GGCACGAAAATGATCTTCGTGGGCATCAAAAAAA AAGAAGAACGCGCGGACCTGATCGCGTACCTG AAAAAGGCGACGAACGAATGA - 3′	*Integrated DNA Technologies (IDT)*	Custom synthesis, https://eu.idtdna.com/
K86A/K87A/K88A Cc-encoding gBlock: 5′ - ATGGGCGACGTGGAAAAGGGCAAAAAGATC TTCATCATGAAATGCTCGCAGTGCCACACGGTG GAAAAAGGCGGCAAACACAAAACCGGTCCCAA CCTGCACGGCCTGTTCGGCCGCAAAACGGGCC AGGCGCCGGGCTACAGCTACACGGCGGCGAA CAAAAACAAAGGCATCATCTGGGGCGAAGACA CGCTGATGGAATACCTCGAGAACCCGAAAAAAT ACATCCCGGGCACGAAAATGATCTTCGTGGGCA TCGCCGCCGCCGAAGAACGCGCGGACCTGATC GCGTACCTGAAAAAGGCGACGAACGAATGA - 3′	*Integrated DNA Technologies (IDT)*	Custom synthesis, https://eu.idtdna.com/
K86R/K87R/K88R Cc-encoding gBlock: 5′ - ATGGGCGACGTGGAAAAGGGCAAAAAGATC TTCATCATGAAATGCTCGCAGTGCCACACGGTG GAAAAAGGCGGCAAACACAAAACCGGTCCCAA CCTGCACGGCCTGTTCGGCCGCAAAACGGGCC AGGCGCCGGGCTACAGCTACACGGCGGCGAA CAAAAACAAAGGCATCATCTGGGGCGAAGACAC GCTGATGGAATACCTCGAGAACCCGAAAAAATA CATCCCGGGCACGAAAATGATCTTCGTGGGCA TCAGGAGGAGGGAAGAACGCGCGGACCTGAT CGCGTACCTGAAAAAGGCGACGAACGAATGA - 3′	*Integrated DNA Technologies (IDT)*	Custom synthesis, https://eu.idtdna.com/

(*Continued on next page*)

Continued

REAGENT or RESOURCE	SOURCE	IDENTIFIER
pET28a(+) expression vector for SET/TAF-Iβ	Martínez-Fábregas et al.[32]	https://doi.org/10.1074/mcp.M113.034322.
pET28a(+) expression vector for Q69C SET/TAF-Iβ	This manuscript	N/A
pET28a(+) expression vector for D226C SET/TAF-Iβ	This manuscript	N/A
pET28a(+) expression vector for E243C SET/TAF-Iβ	This manuscript	N/A
pET28a(+) expression vector for D260C SET/TAF-Iβ	This manuscript	N/A
pET28a(+) expression vector for D277C SET/TAF-Iβ	This manuscript	N/A
pET28a(+) expression vector for NPM1	González-Arzola et al.[34]	https://doi.org/10.1038/s41594-022-00842-3
pET14b expression vector for SET/TAF-Iβ ΔC	Muto et al.[39]	https://doi.org/10.1073/pnas.0603762104
pET14b expression vector for Q69C SET/TAF-Iβ ΔC	Casado-Combreras et al.[44]	https://doi.org/10.1016/j.csbj.2022.07.009
pBTR1 expression vector (Cc)	Olteanu et al.[107]	Addgene RRID: Addgene_22468
pBTR1 expression vector for K5A/K7A/K8A Cc	This manuscript	N/A
pBTR1 expression vector for K86R/K87R/K88R Cc	This manuscript	N/A
pLW01 expression vector (Cc)	Pecina et al.[110]	https://doi.org/10.1021/bi100486s
pLW01 expression vector for K5R/K7R/K8R Cc	This manuscript	N/A
pLW01 expression vector for K86A/K87A/K88A Cc	This manuscript	N/A
Software and algorithms		
Spectra Manager	*Jasco*	https://jascoinc.com/products/spectroscopy/molecular-spectroscopy-software/
SEQUEST™ HT search engine	*Thermo Scientific*	https://www.thermofisher.com/es/es/home/industrial/mass-spectrometry/liquid-chromatography-mass-spectrometry-lc-ms/lc-ms-software/multi-omics-data-analysis/proteome-discoverer-software.html
Nano Analyze	*TA Instruments*	https://www.tainstruments.com/soporte/software-downloads-support/?lang=es
TopSpin NMR software (version 4.0.6)	*Bruker*	https://www.bruker.com/en/products-and-solutions/mr/nmr-software/topspin.html
OpenMM	Eastman et al.[111]	https://openmm.org/
AMBER 16 package	Case et al.[112]	https://ambermd.org
UCSF Chimera 1.15	Pettersen et al.[113]	https://www.cgl.ucsf.edu/chimera/
Adaptive Poisson-Bolzmann Solver (APBS, version 3.4.1, web server)	Jurrus et al.[114]	https://server.poissonboltzmann.org/
PDB2PQR (version 3.6.1, web server)	Dolinsky et al.[115]	https://server.poissonboltzmann.org/
MODELLER	Webb and Sali[58]	https://salilab.org/modeller/
LAS X	*Leica Microsystems*	https://www.leica-microsystems.com/products/microscope-software/
LAS-AF	*Leica Microsystems*	https://www.leica-microsystems.com/products/microscope-software/
FIJI (ImageJ)	Schindelin et al.[116]	https://fiji.sc/
Origin 2018b	*OriginLab Corporation*	https://www.originlab.com/index.aspx?go=PRODUCTS/Origin
Other		
HisPur™ Ni-NTA resin	*Thermo Scientific*	Cat. n.: 88222
Foresigth Nuvia S 5 mL column	*BioRad*	Cat. n.: #7324743
3 kDa/10 kDa cut-off Amicon Ultra™ centrifugal filters	*Merck Millipore*	Cat. n.: UFC9003/UFC9010
PD-10 desalting columns	*GE Healthcare/Cytiva*	Cat. n.: GE17-0851-01

RESOURCE AVAILABILITY

Lead contact

Further information and requests for resources and reagents should be directed to and will be fulfilled by the lead contact, Prof. Irene Díaz-Moreno (idiazmoreno@us.es).

Materials availability

SET/TAF-Iβ and cytochrome *c* clones, and all resources will be made available upon request.

Data and code availability

- All data will be shared by the lead contact upon request.
- This paper does not report original code.
- Any additional information required to reanalyze the data reported in this paper is available from the lead contact upon request.

METHOD DETAILS

DNA constructs

For recombinant expression of full-length SET/TAF-Iβ, SET/TAF-Iβ ΔC and NPM1, plasmids previously constructed were used.[32,34,39] Genes encoding the abovementioned constructs were subcloned along with an N-terminal 6xHis tag, into a pET28a(+)—SET/TAF-Iβ and NPM1—or a pET14b—SET/TAF-Iβ ΔC—under the T7 promoter.

Cys single residues were introduced by single mutations at different positions in SET/TAF-Iβ to graft the MTSL nytroxide probe. Site-directed mutagenesis was performed by polymerase chain reaction (PCR), using the pET28a(+)-SET/TAF-Iβ construct. The following primers were designed: 5′-CCAACCATTTTTTTGCAAGAGGTCAGAA-3′ and 5′-TTCTGACCTCTTGCAAAAAAATGGTTGG-3′ for the Q69C mutation; 5′-GTTCCCGATATGTGTGATGAAGAAGG-3′ and 5′-CCTTCTTCATCACACATATCGGGAAC -3′ for D226C; 5′-GATGAAGAGGAG TGCGGATTAGAAGAT-3′ and 5′-ATCTTCTAATCCGCACTCCTCTTCATC-3′ for E243C; 5′-GAAGGTGAAGAATGTGAAGATGATGATG-3′ and 5′-CATCATCATCTTCACATTCTTCACCTTC-3′for D260C; and 5′-GAAGGAGAAGATTGCTAACTCGAGCAC-3′ and 5′-GTGCTCGAGT TAGCAATCTTCTCCTTC-3′for D277C.

The DNA encoding for Cc was already cloned into the pBTR1 expression vector, along with the *CYC3* gene, encoding for yeast heme lyase for the proper heme group assembly and protein folding.[107]

The Cc K5A/K7A/K8A mutant was obtained by three successive steps of site-directed mutagenesis, using PCR with the primers 5′-GACGTGGAAAAGGGCGCGAAGATCTTCATCATG-3′ and 5′-CATGATGAAGATCTTCGCGCCCTTTTCCACGTC-3′ to mutate Lys7, secondly 5′-GCGCGGCGATCTTCATCATGAAATGCTCGCAGTGCCACA-3′ and 5′-AGATCGCCGCGCCCTTTTCCACGTCGCCC-3′ to mutate Lys8, and finally 5′-CGACGTGGAAGCGGGCGCGGCGATCTTC-3′ and 5′-GAAGATCGCCGCGCCCGCTTCCACGTCG-3′ for Lys5 replacement.

For the construction of expression plasmids for K5R/K7R/K8R and K86A/K87A/K88A Cc mutants, gBlocks for each of the genes were acquired from Integrated DNA Technologies, Inc (IDT). Such DNAs were amplified by PCR with the primers 5′-CCATGGATGGGCGACGTGG-3′ and 5′-GGATCCTCATTCGTTCGTCGCC-3′, and subcloned into the pLW01 bacterial expression vector,[110] using NcoI and BamHI restriction enzymes (*New England Biolabs*).

The gene encoding the Cc K86R/K87R/K88R mutant was amplified using the oligonucleotides 5′-GAAGGAGATATATCCATGGGCGA CGTGGAAAAG-3′ and 5′-CATCTTGGTACCTTATCATTCGTTCGTCGCCTTT-3′ and cloned into a linearized pBTR1 vector using the In-Fusion™ Snap Assembly EcoDry system (*Takara Bio*). pBTR1 was linearized by PCR with the primers 5′-TAAGGTACCAAGATGG-3′ and 5′-GGATATATCTCCTTCTTAAAG-3′.

Protein expression and purification

SET/TAF-Iβ full-length and ΔC constructs, their respective Q69C mutants, D226C, E243C, D260C and D277C SET/TAF-Iβ, and NPM1 were expressed in the *E. coli* BL21(DE3) strain. Firstly, lysogeny-broth (LB) pre-cultures supplemented with kanamycin (50 μg/mL)—for full-length SET/TAF-Iβ and NPM1—or ampicillin (100 μg/mL)—for SET/TAF-Iβ ΔC constructs expression—were grown at 37°C up to saturation. Afterward, they were used to inoculate the final cultures, which were grown at 37°C until an optical density measured at 600 nm (OD_{600}) of 0.6–0.8 was reached. 1 mM isopropyl-β-D-1-thiogalactopyranoside (IPTG) was then added to induce protein expression over night at 30°C.

WT Cc and K5A/K7A/K8A mutant were expressed in the *E. coli* BL21(DE3) strain, as previously described.[117] Briefly, LB precultures supplemented with ampicillin (100 μg/mL) were grown at 37°C up to saturation. Then, 2.5 mL were used to inoculate 2.5 L cultures in 5 L Erlenmeyer flasks. For the expression of the K86R/K87R/K88R variant, single colonies were inoculated in 4 L LB cultures contained in 5 L Erlenmeyer flasks, so as to get semi-anaerobic growth conditions. These cultures were incubated over night at 30°C under agitation. The expression of Cc K5R/K7R/K8R and K86A/K87A/K88A mutants was performed in C43(DE3) *E. coli* cells. Terrific-broth (TB) precultures supplemented with ampicillin (100 μg/mL) and 1% glucose were grown at 37°C up to saturation. Then, TB 1 L cultures contained in 2 L Erlenmeyer flasks were inoculated with 5 mL of preculture and grown at 37°C until an OD_{600} of 0.6–0.8. Expression was induced with 0.5 mM IPTG and cultures were incubated over night at 30°C.

After expression, cells were harvested by centrifugation at 4,500 × *g* for 10 min (4°C) and then, resuspended in lysis buffer, consisting on 20 mM Tris-HCl buffer (pH 8.0), 800 mM NaCl and 10 mM imidazole for SET/TAF-Iβ and NPM1 proteins or 10 mM tricine-NaOH (pH 8.5) for C*c* constructs. Cell suspensions were treated during 15 min at room temperature with 0.2 mg/mL lysozyme and 0.02 mg/mL DNase I, in the presence of 0.01% phenylmethylsulfonyl fluoride (PMSF) and cOmplete™ Mini, EDTA-free, protease-inhibitor mixture (*Roche*). Then, cells were sonicated for 4 min (30''/45'' cycles, 35% amplitude). Cellular debris was removed by centrifugation at 48,000 × *g* for 30 min (4°C).

SET/TAF-Iβ and NPM1 constructs were purified from the protein extracts by affinity chromatography, using a HisPur™ Ni-NTA resin (*Thermo Scientific*) precharged column. For SET/TAF-Iβ Cys mutants, 5 mM dithiotreitol (DTT) was present during both bacterial lysis and protein purification. C*c* purification was based on cation exchange chromatography, using a *Foresigth Nuvia S* 5 mL column (*BioRad*). The purity and homogeneity of protein preparations were tested by SDS-PAGE. SET/TAF-Iβ and NPM1 protein concentrations were measured by the Bradford method.[118] C*c* concentrations were determined by UV-Vis spectrophotometry, using an extinction coefficient at 550 nm of 28.92 mM^{-1} cm^{-1} for the reduced state of the hemeprotein. Proteins were concentrated using 3 or 10 kDa cut-off *Merck Millipore* centrifugal filters and dialyzed against 10 mM sodium phosphate buffer (pH 7.4).

Circular dichroism spectroscopy

CD spectra of the WT and mutants C*c* were recorded at 20°C in the far UV region (190–250 nm) or in the visible (300–600 nm) at 0.2 nm/min, using a 1-mm thick quartz cuvette on a J-815 CD Spectropolarimeter (*Jasco*), equipped with a Peltier temperature control system. Measurements were taken for 10 μM C*c* in the far UV or 30 μM C*c* in the visible region. In all cases, samples were in 10 mM sodium phosphate (pH 7.4) buffer, containing a 10-fold molar excess of potassium hexacyanoferrate (III). Twenty scans were averaged for each sample.

Mass spectrometry

Mass spectrometry assays were performed at the Biomolecular mass, proteomics and metabolomics (BIO-MS) laboratory at the University Pablo de Olavide.

For in-solution protein samples, measurements were performed using a MALDI-TOF Ultraflextreme system (Bruker) configured on positive linear mode. For each spectrum, results of 3,000 laser shots were averaged. A 1:10 mixture of α-cyano-hydroxycinnamic acid and 2,5-dihydroxybenzoic acid (20 mg/mL) was used as MALDI matrix. This matrix was in turn mixed with the sample, in a 1:2 (v/v) ratio and 0.5 μL were deposited on a film of α-cyano-hydroxycinnamic acid and air-dried at RT.

To identify the corresponding mutations of each Cc variants, they were subjected to tryptic digestion. Acrylamide gel bands were detained with ammonium bicarbonate and acetonitrile. DTT and iodoacetamide were respectively used to break disulphide bonds and carbamidomethylate cysteine residues. Samples were incubated overnight at 37 °C with bovine trypsin or at room temperature with chymotrypsin (K5R/K7R/K8R mutant), at ratio 1:10 (enzyme:substrate). After acetonitrile extraction and acidification, samples were desalted and concentrated with C18-filled tips.

Fingerprint MALDI measurements on C*c* K86A/K87A/K88A and K86R/K87R/K88R mutants, positive reflectron mode was used. The results of 3000 lasedata-dependent acquisitionpectrum. Measurements on C*c* K5A/K7A/K8A and K5R/K7R/K8R mutants were performed with an Orbitrap Q-Exactive Plus mass spectrometer coupled to an Easy-nLC liquid nanochromatograph (Thermo Scientific).false-discovery rates were separated using a 50 cm C18 EASY-Spray column coupled with a C18 PepMap100 2 cm pre-column. A non-linear gradient was used between phase A (0.1% formic acid) and phase B (80% acetonitrile, 20% water, 0.1% formic acid) during 120 min in reverse phase mode. Then, top 10 MS/MS spectra were acquired in data-dependent acquisition (DDA) mode. Spray voltage was fixed at 2.9 kV and capillary temperature at 300°C. Maximum IT was set at 30 ms.

LC-MS data were analyzed using the SEQUESTTM HT search engine (Thermo Scientific). The following amino acid modifications were considered in the analysis: static carbamidomethylation (Cys), dynamic oxidation (Met) and dynamic acetylation (N-termini). Data were searched against specific protein sequences for each mutant and results were filtered using a 0.01% protein false-discovery rate (FDR) threshold.

Protein spin labeling

SET/TAF-Iβ Cys mutant samples were dialyzed against 20 mM sodium phosphate (pH 7.4) and 50 mM NaCl, containing 1 mM of DTT. After the removal of DTT by gel filtration with a desalting PD-10 column (*GE Healthcare*), the nitroxide spin label MTSL ([1-oxyl-2,2,5,5-tetramethyl-δ3-pyrroline-3-methyl] methanethiosulfonate; *Toronto Research Chemicals Inc.*, Toronto, Canada) was added to the sample at 7 to 10-fold molar excess from concentrated stock solutions in acetonitrile. The labeling reaction was carried out at 4°C, in the dark, under gentle stirring and continuous flow of Ar during 1 h. Excess of unbound label was removed using a desalting column (PD-10) in 10 mM sodium phosphate, pH 6.3. The fractions containing the labeled variants were pooled and concentrated using 30 kDa cut-off *Merck Millipore* centrifugal filters.

Electron paramagnetic resonance

CW-EPR experiments were performed on spin-labeled SET/TAF-Iβ single-Cys mutants, in both the absence and the presence of reduced C*c* in a 1:2 SET/TAF-Iβ:C*c* molar ratio. EPR spectra were recorded at 23°C on an ELEXSYS E500 *Bruker* spectrometer, equipped with a Super High Q Sensitivity resonator, operating at X-band (9.9 GHz). The microwave power was 10 mW, the magnetic field modulation amplitude 0.1 mT

and the frequency modulation 100 kHz. Spin concentration was obtained by measuring the double integral of EPR signals, compared to a reference sample. Spin-labeling yields ranging from 80 to 100% were obtained for all variants.

Nuclear magnetic resonance

1D ^{1}H NMR spectra of the reduced Cc variants were acquired on a *Bruker* Avance III 500 MHz, equipped with a 5 mm TCI cryoprobe, at 25°C. All samples contained 50 μM protein and 250 μM sodium ascorbate to ensure Cc was in a fully reduced state. Experiments were performed in 10 mM sodium phosphate buffer pH 7.4, containing 5% D_2O to adjust the lock signal. Water signal was suppressed by excitation sculpting method.[119] Spectra acquisition and processing were made using TopSpin NMR software (*Bruker*).

Molecular dynamics computations

MD computations on Cc variants were performed with the OpenMM software[111] in a CUDA platform. The initial structure of WT Cc was taken from the NMR model of human reduced Cc (PDB entry 2N9I [107]). The models of simulated mutants were built based on the WT protein structure. All the topology and coordinate files were generated by using the LEAP module of the AMBER 16 package[112] and the ff19SB force-field libraries.[108] Force-field parameters for the heme group[109] were used to generate topology and coordinates.

Simulations were performed under periodic boundary conditions, using an orthorhombic cell geometry and particle mesh Ewald (PME) electrostatics with an Ewald summation cut off of 1 nm. The system was neutralized with chloride counter-ions according with the total charge of the protein and solvated using an optimal 3-charge, 4-point rigid water model (OPC) molecules.[120] For each system, evolution times of 1 μs were simulated at 298 K and 1 atm, with 2,500 previous energy minimization steps of 2 fs using a Langevin integrator[121] with a friction coefficient of 1 ps^{-1}.

The CPPTRAJ module of AMBER[122] was used for trajectory analysis. Molecular graphics were made with the UCSF Chimera 1.15 software.[113]

Electrostatic surface potential computations

The ESPs of SET/TAF-Iβ and the different Cc variants were calculated using the Adaptive Poisson-Bolzmann Solver (APBS, version 3.4.1)[114] at 15 mM ionic strength. To do that, a structural model of SET/TAF- Iβ was built using MODELLER[58] to construct the absent stretches in the crystallographic structure (PDB entry 2E50[39]). For Cc, structures resulting from 1-μs MD simulations of the WT protein and each mutant were used. Structures were prepared for APBS calculations by using the PDB2PQR (version 3.6.1) tool.[115] Surface mappings were made using the UCSF Chimera 1.15 software.[113]

Isothermal titration calorimetry

ITC experiments were performed in a Nano ITC Low Volume (*TA Instruments*) at 25°C. The experiments consisted of 20 injections of 300 μM solutions of reduced WT or mutant Cc, 2.5 μL each. The sample cell was initially filled with 20 μM SET/TAF-Iβ or NPM1. All the experiments were performed in 10 mM sodium phosphate buffer pH 7.4, in the presence of 100 mM NaCl in titrations involving NPM1 so as to maintain is pentameric state.[55] Injection interval was set to 180 s, allowing the return of the thermal power signal to the baseline before the next injection. During the titration, stirring was constantly maintained at 300 rpm. The reference cell was filled with ultra-pure water and all samples were degassed prior to the experiments. Injection heats normalized per mole of injectant versus molar ratio data were fitted to a set of independent and identical binding sites model or a two cooperative-binding sites model (see Note S1).

Protein fluorescent labeling

Fluorescent labeling of SET/TAF-Iβ variants and NPM1 was performed by taking advantage of Cys residues to graft the fluorescent Oregon Green™ 488 maleimide probe (*Molecular Probes*). SET/TAF-Iβ proteins labeling required the usage of their Q69C mutant, as the WT proteins lack Cys residues. NPM1 is labeled on its exposed Cys104. Proteins were dialyzed in 20 mM sodium phosphate (pH 7.4), 100 mM NaCl and 1 mM DTT. Then, DTT was removed by gel filtration using a desalting PD-10 column (*GE Healthcare*). Immediately, fluorescent probe was added at 10-fold molar excess from a concentrated stock solution in DMSO and the labeling reaction was performed for 2 h at RT in the dark, in 20 mM sodium phosphate buffer (pH 7.4) and 100 mM NaCl.

Cc WT and mutant variants were labeled with the Texas Red™-X succinimidyl ester probe (*Molecular Probes*), which conjugates with non-protonated primary amine groups. Labeling reaction was carried out in 20 mM HEPES at pH 7.0, in order to maximize the protonation of Lys ε-amine groups and then restrict the labeling to the N-terminus of the protein. The reaction was incubated under agitation during 2 h at RT.

Excess of unbound labels was removed by extensive dialysis in 10 mM sodium phosphate (pH 7.4) buffer. Labeled proteins were concentrated in 10 kDa cut-off *Amicon Ultra*™ centrifugal filters (*Merck*). Protein concentration and degree of labeling were determined by recording UV-visible spectra and following the manufacturer's indications.

Phase separation assays and imaging

Droplet formation was performed by mixing unlabeled SET/TAF-Iβ, SET/TAF-Iβ ΔC or NPM1 at a final concentration of 10 μM with Cc variants at the indicated molar ratios, in 10 mM sodium phosphate (pH 7.4) buffer. When specified, a final concentration of 50 or 100 mM NaCl, or 15% Ficoll™ PM70 (*Cytiva*) was included. For fluorescence droplet analysis, fluorescently-labeled proteins were included in samples to represent 10% of the respective partner. The samples were equilibrated at RT for 5 min and then mounted in sealed chambers, composed of a glass

slide and coverslip and kept together by a layer of pierced 3M™ double-sided, 100-μm thick tape. Once mounted, samples were equilibrated again during 10 min.

Samples were imaged at RT at a Leica DM6000B (*Leica Microsystems*) fluorescence microscope, using a 40× objective and an ORCA-ER camera (Hamamatsu). Differential interference contrast (DIC) and fluorescence filters FITCL5 filter (excitation band-pass, 480/40; emission band-pass, 527/30) and a Tx2 filter (excitation, 560/40 nm; emission, 645/75 nm) to visualize Oregon Green™ 488 and Texas Red™, respectively were used when indicated. Images were processed and analyzed with the LAS X (*Leica Microsystems*) and the FIJI (ImageJ)[116] software packages.

Fluorescence recovery after photobleaching

Samples for FRAP measurements in liquid condensates were prepared as described in the previous section. Experiments were performed by a Leica TCS SP5 (*Leica Microsystems*) laser-scanning confocal microscope, using a 63×/1.4 oil immersion objective. Droplets suitable for FRAP measurements were preselected.

ROIs of 0.854 × 0.787 μm covering a fraction of the selected condensate were bleached first with the 561-nm and then with the 488-nm laser lines—to avoid FRET-induced artifactual bleaching on the red channel—at 40% or 100% laser power, respectively. The bleaching protocol was as follows: three pre-bleaching images, five bleaching pulses at the indicated laser power and 100 post-bleaching images were taken every 774 ms. Images were collected using the Leica LAS-AF (*Leica Microsystems*) software, recording emitted fluorescence between 592 and 632 nm for the red channel and between 497 and 552 nm for the green channel.

Mean fluorescence-intensity of ROIs inside bleached droplets and regions around them (as a control) were measured before and after bleaching. As well, mean fluorescence intensity of nonbleached droplets and the background fluorescence outside droplets were also recorded as controls. Fluorescence intensities were measured using the FIJI (ImageJ)[116] software package.

The normalized intensity was plotted over the time in the different FRAP determinations, analyzing five droplets for each protein complex. Normalized intensity over the time was fitted to a single exponential function ($y = y_0 + A*(1-e^{-kt})$), being "A" the plateau intensity and "k" a fitting constant. Recovery half times were calculated as ln(0.5)/-k. Curve fittings and calculations were made using Origin 2018b (*OriginLab Corporation*).

QUANTIFICATION AND STATISTICAL ANALYSIS

Phase separation assays

For droplet quantification, 10 images were acquired and quantified per assayed protein complex. The mean and standard deviation (SD) of droplet-occupied area were calculated. Images were processed and analyzed using the LAS X (*Leica Microsystems*) and the FIJI (ImageJ)[116] software packages.

Fluorescence recovery after photobleaching

For FRAP measurements, the normalized intensity was plotted over time, analyzing five droplets for each protein complex. Normalized intensity over time was fitted to a single exponential function ($y = y_0 + A\ (1-e^{-kt})$), being "A" the plateau intensity and "k" a fitting constant. Recovery half times were calculated as ln(0.5)/-k. Resulting parameters are presented as the mean ± standard error of the mean (SEM). Images were processed and analyzed using the LAS X (*Leica Microsystems*) and the FIJI (ImageJ)[116] software packages. Data processing and fitting were performed using Origin 2018b (*OriginLab Corporation*).

Molecular dynamics: H-bonds calculations

Both the inter-residue (corresponding to Lys clusters) and the total intramolecular H-bonds information was extracted from 1-μs MD trajectories, which were analyzed using the CPPTRAJ module of AMBER.[122] Then mean and SD were calculated for both datasets and for each Cc variant.